Received: 16 April 2022 | Revised: 12 December 2022 | Accepted: 9 January 2023

DOI: 10.1002/suco.202200378

ARTICLE

fib CEB-FIP WILEY

Seismic vulnerability assessment of reinforced concrete bridge piers with corroded bars

Dario De Domenico | **Davide Messina** | **Antonino Recupero**

Department of Engineering, University of Messina, Messina, Italy

Correspondence
Dario De Domenico, Department of Engineering, Contrada Di Dio, 98166 Sant'Agata, University of Messina, Messina, Italy.
Email: dario.dedomenico@unime.it

Abstract

Reinforced concrete (RC) structures located in aggressive environment, for example, RC bridge piers close to the sea and experiencing chloride attacks, may be exposed to an increased seismic vulnerability. This requires practical yet effective safety assessment strategies aimed to determine the seismic behavior by incorporating corrosion deterioration phenomena. An easy-to-use phenomenological model is here developed to describe the seismic behavior of corroded RC elements based on a fiber hinge formulation wherein the corrosion-induced mechanical degradation of concrete and steel is implemented through appropriate constitutive laws at the fiber level. The developed fiber hinge formulation is first validated against experimental cyclic tests of corroded RC columns from the literature. Then, the proposed approach is used for the seismic vulnerability assessment of the Zappulla multi-span viaduct (southern Italy), whose RC bridge piers (with a box-shaped, two-cell hollow rectangular cross section) are exposed to carbonation and chloride-induced corrosion. A comprehensive in-situ testing campaign is conducted for the mechanical characterization of the materials in the RC piers. Corrosion potential mapping, carbonation tests and tensile tests on corroded bars extracted from RC piers are critically interpreted to calibrate the constitutive laws of the fiber-hinge model. Motivated by experimental findings, numerical seismic analyses (including linear dynamic, nonlinear static and nonlinear dynamic analyses) are performed under two different corrosion scenarios to quantify the impact of corrosion on the resulting seismic vulnerability conditions of bridge piers with corroded bars. The proposed approach is characterized by low computational cost and lends itself to large-scale seismic vulnerability assessment of other existing RC bridges placed in corrosive environment.

KEYWORDS

carbonation tests, corroded bars, corrosion, corrosion potential mapping, cyclic behavior, fiber hinge model, finite element analysis, RC bridge piers, seismic response, seismic vulnerability assessment

1 | INTRODUCTION

Many existing reinforced concrete (RC) structures were constructed more than 50 years ago. Besides the changed design standards and philosophy in comparison to the regulations in force today, attention to durability aspects in past projects was not always considered a crucial performance objective as in current design process. Moreover, the vulnerability of such existing structures is further amplified by material degradation process that might take place over the structural lifetime. Corrosion is one of the most frequent deterioration phenomena occurring in existing RC structures located in harsh environments (e.g., exposure to sulphate and chloride attacks) and is responsible for significant alteration (reduction) of the structural safety unless carefully prevented and controlled. In addition to the reduction of the resistant cross-sectional area of corroded steel bars, there are other indirect effects caused by corrosion in RC structures, such as diffuse microcracking of concrete in the neighborhood of the corroded bar (induced by the larger volume occupied by rust and oxides in comparison to the uncorroded metal), spalling of concrete cover, deterioration of bond behavior at the concrete-corroded bar interface and decrease of concrete compressive strength induced by carbonation. Additionally, a concurrent aspect concerns the reduction of the confinement action of transverse corroded reinforcement, which leads to a reduction of structural ductility and considerably increases the vulnerability of corroded structures located in earthquake-prone regions.

In this context, a topical research line concerns the investigation of the influence of corrosion on the alteration of the load-bearing capacity and structural ductility of RC elements under seismic loading. Cyclic experimental tests on RC columns[1–6] were carried out considering different corrosion levels. Based on available experimental findings, numerical models were developed to perform seismic vulnerability assessment of corroded RC buildings[7,8] and bridges.[9–12]

The process of chloride-induced corrosion includes three main phases that are initiation, propagation, and deterioration phase.[13] Modeling each of these phases and their mutual relationships involves complex time-dependent multi-physics models, by solving appropriate differential evolution equations and taking into account suitable boundary conditions.[14] As an alternative, instead of simulating the complex corrosion process at a microstructural level by accounting for time-dependent degradation laws, macroscopic phenomenological models can be adopted by focusing only on the effect of corrosion on the global structural behavior of RC element. This is the approach pursued in this paper, which develops an easy-to-use phenomenological model through a fiber hinge approach wherein appropriate constitutive laws are adopted for cover concrete, core concrete, and corroded steel reinforcing bars at the fiber level. The model is first validated against experimental cyclic tests of corroded RC columns from the literature, in which the level of corrosion of longitudinal bars was measured on bare and embedded bars. The comparison between experimental and numerical model is performed in terms of overall hysteretic behavior, namely backbone, maximum strength, and strength degradation over repeated cycles. The proposed fiber hinge model is then utilized for the seismic vulnerability assessment of the Zappulla multi-span viaduct (southern Italy), here analyzed as a case study. Experimental measures of the corrosion potential performed in situ revealed a state of widespread corrosion in the box-shaped RC piers of this viaduct. A comprehensive in-situ testing campaign is conducted for the mechanical characterization of the materials in the piers, including carbonation tests, concrete coring, sclerometric tests combined with ultrasonic pulse velocity for concrete compressive strength determination, pachometer tests, corrosion potential mapping and extraction of steel bars for tensile tests. The experimental findings are employed for calibrating the fiber-hinge model of the RC piers, which is used to perform linear dynamic, nonlinear static and nonlinear dynamic analyses under two different corrosion scenarios to quantify the impact of corrosion on the resulting safety conditions of bridge piers under seismic loading.

2 | CORROSION-INDUCED DEGRADATION OF MATERIAL PARAMETERS IN RC STRUCTURES

In the literature, many empirical relationships and mechanistic models were developed and calibrated from experimental results on corroded bars (bare or embedded in concrete) tested under monotonic tensile tests,[15–24] fatigue tests[19,22,25] and bending tests on RC beams with corroded reinforcing bars[26,27] to predict the corrosion-induced degradation of material parameters in RC structures. Three main strategies have been adopted to generate corrosion in such experimental samples: (1) service corrosion, concerning bars naturally corroded in open air[15,17–19,26,28]; (2) accelerated corrosion, either through an impressed current intensity adjusted to achieve a desired mass loss in a reasonably specified time through Faraday's law,[16,19,20,25,26,29] or through laboratory salt spray exposure[21,22]; (3) pitting (localized) corrosion, in most cases simulated by machining hemispherical cavities (indentation process) on reinforcing bars.[16,23,24,30]

Ductility and strength of corroded RC elements (e.g., building columns or bridge piers) decrease for different factors: (1) degradation of corroded stirrups yield force, which reduces the confinement action on the

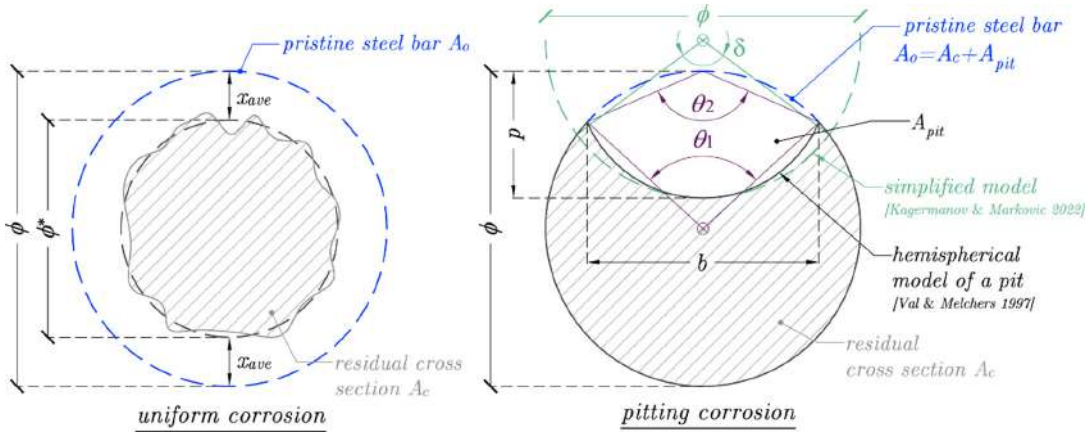

FIGURE 1 Scheme of residual cross section of single bar (shaded area) under uniform (left) and pitting (right) corrosion

concrete section; (2) degradation of strength and deformation capacity of corroded longitudinal bars[16,31,32]; (3) formation of a gap between longitudinal and transversal reinforcing bars, which amplifies the longitudinal bar free length and, in turn, the buckling attitude of reinforcing bars,[33] thus further reducing the effectiveness of confinement[34]; (4) corrosion-induced degradation of concrete compressive strength,[35] especially in the area close to the corroded bars,[7] including cracking and spalling of concrete cover[36–39]; (5) bond degradation.[40,41]

The most relevant effect of corrosion is the steel cross-section loss, which is calculated through gravimetric methods as per the ASTM code[42] after cleaning the corroded bar and removing corrosion products. The average mass loss (or corrosion degree with respect to the original mass) is:

$$\Delta m = \frac{m_o - m}{m_o} \tag{1}$$

where m_o and m denote the mass of uncorroded and corroded bar, respectively. The corrosion attack penetration can be quantified through the reinforcement diameter decrease. Based on Refs.36,38,43 and considering the sketch in Figure 1, a unified formulation can be obtained for both uniform and pitting corrosion as follows [Equation (2)]:

$$\phi^* = \phi - \kappa \times x_{ave} \tag{2}$$

where ϕ and ϕ^* represent the uncorroded and the "equivalent corroded" diameter (assuming circular cross section after corrosion) and κ is the so-called pit concentration factor[44] that quantifies the ratio between the maximum pit depth p and the average (i.e., "uniform") corrosion penetration x_{ave} calculated indirectly from weight loss.[38] Typical κ values vary from 4 to 8 and from 5 to 13 for naturally and accelerated corroded bars, respectively. For homogeneous (uniform) corrosion $\kappa = 2$, then $\phi^* = \phi - 2 \times x_{ave}$ (cf. Figure 1 left). The average attack penetration x_{ave} can be linked to the average mass loss of Equation (1) through[36]:

$$x_{ave} = \frac{\phi}{\kappa}\left(1 - \sqrt{1 - \Delta m}\right) \tag{3}$$

Pitting corrosion varies randomly along the bar, and pits of different forms can be observed in practice. However, for simplicity, in the literature pitting corrosion was often studied through an idealized hemispherical form of a pit with radius p, as proposed by Val & Melchers[43] (see Figure 1 right):

$$A_{pit}(\theta_1, \theta_2) = \begin{cases} A_1 + A_2 & p \le \dfrac{\phi}{\sqrt{2}} \\ A_0 - A_1 + A_2 & \dfrac{\phi}{\sqrt{2}} < p \le \phi \\ A_0 & p \ge \phi \end{cases} \tag{4}$$

where p is the pit depth, $b = 2p\sqrt{1 - (p/\phi)^2}$ the pit width, $A_0 = \pi\phi^2/4$ the cross-sectional area of the pristine (uncorroded) steel bar, $A_1 = 0.5\left(\theta_1 \left(\frac{\phi}{2}\right)^2 - b\left|\frac{\phi}{2} - \frac{p^2}{\phi}\right|\right)$, $A_2 = 0.5(\theta_2 p^2 - b p^2/\phi)$, $\theta_1 = 2\arcsin(b/\phi)$, $\theta_2 = 2\arcsin(0.5b/p)$. The normalized area of the pit A_{pit}/A_0 is plotted in Figure 2 (left) and compared to a simpler equation proposed by Kagermanov and Markovic[45] in which A_{pit} represents the overlapping area between two circles of diameter ϕ penetrating a depth p, that is:

$$A_{pit}(\delta) = \frac{\phi^2}{4}(\delta - \sin\delta) \tag{5}$$

It can be observed that Equation (5) provides a pit area that is slightly overestimated (slightly underestimated) in comparison to that computed via

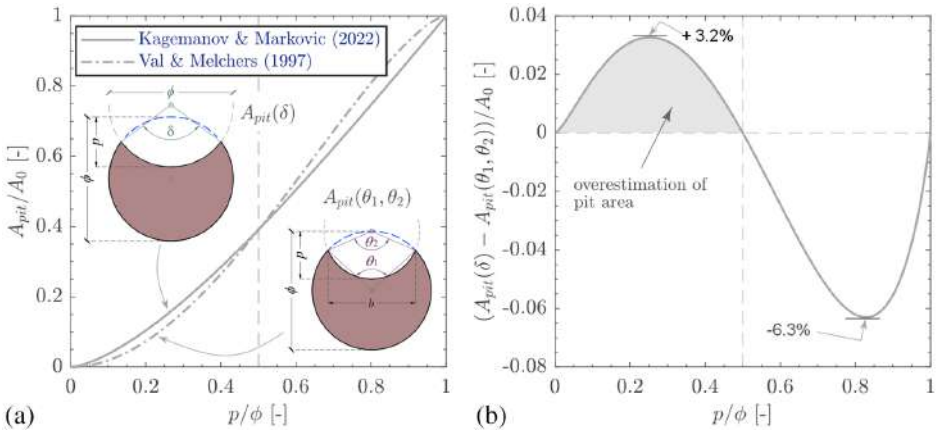

FIGURE 2 Normalized pit area as a function of normalized pit depth for Val and Melchers (1997) versus Kagemanov and Markovic (2022) equation (left), and relative discrepancy between the two formulations (right)

Equation (4) in the range $p < 0.5\phi$ ($p > 0.5\phi$), with maximum overestimation of around 3% (maximum underestimation of around 6%).

The way the corrosion affects the mechanical properties of steel bars is different depending on whether uniform or pitting corrosion takes place. For bars undergoing uniform (generalized) corrosion, the average mass loss Δm mainly governs the degradation of mechanical properties. In particular, the value of a generic mechanical property X (be it a stress measure, a force, a strain value, etc.) is altered (reduced) into a new value $X^* = X^*(\Delta m)$ based on a particular empirical degradation law. As an example, in the literature a simple linear decaying model[16,19,21,29] was proposed for yield and ultimate strength degradation of corroded bars. Since such strengths parameters refer to the reduced cross-sectional area of the corroded bar, to avoid misunderstanding it is more appropriate to refer to yield load F_y and ultimate load F_u of the bar (rather than to yield strength and ultimate strength)[46] as follows, respectively:

$$\frac{F_y^*}{F_y} = 1 - \beta_{F_y} \times \Delta m; \quad \frac{F_u^*}{F_u} = 1 - \beta_{F_u} \times \Delta m \tag{6}$$

Several empirical values of β_{F_y} were determined in the literature through statistical regression of available experimental results, ranging from 0.0050 up to 0.0198,[7] depending on the average corrosion degree Δm, the nature of exposure (service-chlorides, service-carbonation, accelerated corrosion, etc.), the typology of bar (smooth vs. ribbed) and its position with respect to concrete (embedded or bare) and the kind of corrosion attack. Similar values of β_{F_u} were also proposed in the literature to quantify the degradation of the ultimate load of the corroded steel bar. In addition to the strength degradation, a reduction of ultimate strain (which might be of interest in the definition of the overall structural ductility) was also noted in experiments,[32] and linear decaying relationships of the same form as Equation (6) were proposed in the literature,[16,28,32] along with alternative exponentially decaying formulations,[47] respectively:

$$\frac{\varepsilon_{su}^*}{\varepsilon_{su}} = 1 - \beta_{\varepsilon_{su}} \times \Delta m; \quad \frac{\varepsilon_{su}^*}{\varepsilon_{su}} = \exp\left(-\widehat{\beta}_{\varepsilon_{su}} \Delta m\right) \tag{7}$$

As an example, values of $\beta_{\varepsilon_{su}} = 0.021$ and $\widehat{\beta}_{\varepsilon_{su}} = 0.0277$ were proposed by Zhang et al.[8] and Imperatore et al.[47] respectively, which provide a comparable value of reduction coefficient $\varepsilon_{su}^*/\varepsilon_{su}$ in the range $20\% < \Delta m < 30\%$.

The above expressions are valid for uniform corrosion. For localized corrosion (as observed in machine-simulated pit damaged samples), the mechanical properties of corroded bars are altered in a more complex way due to strain localization around the pit. In such cases the corrosion morphology plays a key role: as an example, a different mechanical behavior was observed between localized pitting corrosion (early corrosion) and extensive pitting corrosion (as corrosion-induced cracks propagate),[31] especially in terms of ultimate elongation. Some authors used spatial-time-variant probabilistic models to describe the non-uniform pitting corrosion pattern[48] and statistical methods to investigate correlations between pit depth, residual area and moments of inertia of the cross section.[49] Some formulations correlate damage with geometric parameters like pit width b and pit depth p, pitting morphology,[24,30] as well as centroid relocation at the damaged section triggering local bending when the corroded bar is subject to tensile load.[23] Although these formulations are certainly accurate in describing the mechanical response of bars with pitting corrosion, for practical applications simplified approaches based either (conservatively) on the minimum bar cross section at any point,[16,24] or on mean section loss along with empirical coefficients[50] have been adopted. Since pitting corrosion produces more severe material degradation

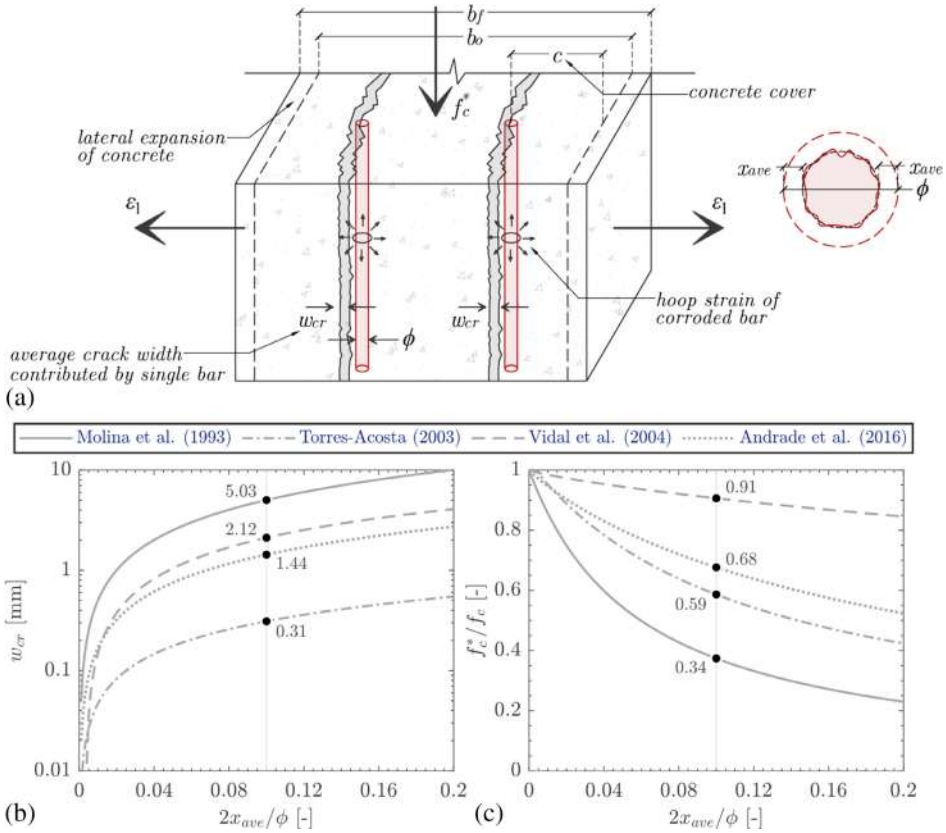

FIGURE 3 Tensile strain of concrete orthogonal to the principal compression stress direction caused by volumetric expansion of corroded bar (a), trend of corrosion-induced crack width (b) and compressive strength reduction (c) as a function of normalized corrosion penetration (cross-sectional properties are taken from corroded RC column tested by Meda et al.[5])

than uniform corrosion[47,51] in terms of strength and ductility characteristics, regression coefficients β are adjusted accordingly.[50]

As better clarified below, the kind of corrosion documented in this work is more pertinent to generalized (rather than localized) corrosion; therefore, empirical degradation relationships of the form of Equations (6)–(7), based on the average mass loss Δm, will be adopted in this paper, in line with literature studies on uniform corrosion. Although this modeling approach is justified in the specific case-study viaduct investigated in this paper, it is worth noting that for large-scale seismic vulnerability assessment of corroded bridge piers (experiencing either uniform or pitting corrosion), the use of empirical (simplified) formulations (over more precise approaches like the ones overviewed above for pitting corrosion) is often required for practical needs due to lacking information on the corrosion morphology of all the bars involved in the pier cross section.

With regard to concrete, volumetric expansion of corroded bars generates tensile strain orthogonal to the principal compression stress direction, longitudinal microcracks (cf. Figure 3a) and reduction of compressive strength (from f_c to f_c^*). This phenomenon, known as compression softening, is also observed in RC members tested under biaxial stress conditions[52] and quantitatively depends on the average tensile strain ε_1. By applying these general concepts to the case of corroded RC members, the formulation proposed by Coronelli and Gambarova[35] describes the corrosion-induced degradation of compressive strength as follows:

$$\frac{f_c^*}{f_c} = \beta_{f_c} = \frac{1}{1 + k\frac{\varepsilon_1}{\varepsilon_{co}}} = \frac{1}{1 + k\frac{(b_f - b_o)}{b_o \cdot \varepsilon_{co}}} \tag{8}$$

In this expression, k is an empirical coefficient that depends on the reinforcing bar roughness and diameter (assumed equal to 0.1 for medium-diameter ribbed bars in the range 10–18 mm) and ε_{co} is the strain at the peak compressive stress of concrete (generally assumed as 0.2%). In Equation (8), the average (smeared) tensile strain ε_1 in the cracked concrete orthogonal to the principal compressive stress direction has been computed as $\varepsilon_1 = (b_f - b_o)/b_o$, where b_o is the original section width in the uncorroded scenario and b_f is the increased section width $(b_f > b_o)$ accounting for corrosion cracking (cf. again Figure 3a). The increase of the section width $(b_f - b_o)$ can be approximated as the product of the number of cracks n (equal to the number of bars in the compressed zone of the section) and the average crack width for each corroded bar w_{cr}, that is:

$$(b_f - b_o) \approx n \times w_{cr} \tag{9}$$

Therefore, introducing Equation (9) into Equation (8), the compressive strength reduction is:

$$\frac{f_c^*}{f_c} = \beta_{f_c} = \frac{1}{1 + k\frac{n \times w_{cr}}{b_o \times \varepsilon_{co}}} \tag{10}$$

The reliability and accuracy of Equation (10) is related to the crack opening w_{cr}, which depends on several factors such as expansive nature of oxides, corrosion degree, concrete cover-to-bar diameter ratio, concrete strength, confinement, to mention only a few. The scatter of results obtained from four literature models of w_{cr}[36–39] is illustrated in Figure 3b), in which we illustrate the trend (in a semi-log plot) of the corrosion-induced crack width w_{cr} as a function of the normalized corrosion penetration $2x_{ave}/\phi$. For this plot, the geometric and mechanical cross-sectional properties of the RC column tested by Meda et al.[5] are assumed (i.e., concrete cover $c = 35$ mm, uncorroded compressive strength $f_c = 20$ MPa, bar diameter $\phi = 16$ mm, section width $b_o = 300$ mm). This corroded RC column is selected in this plot because it will be analyzed in Section 4 for validating the proposed fiber-hinge model. Meda et al.[5] reported an experimental value of the average mass loss $\Delta m = 20\%$ for the four longitudinal (ϕ16) corroded bars of the cross section, which corresponds to an average corrosion penetration x_{ave}, calculated through Equation (3), equal to 0.845 mm, and a normalized corrosion penetration $2x_{ave}/\phi$ of around 0.10. The four models depicted in Figure 3b provide a wide range of w_{cr}, namely 5.03 mm (Molina et al.[39]), 0.31 mm (Torres-Acosta & Martínez-Madrid[38]), 2.12 mm (Vidal et al.[36]) and 1.44 mm (Andrade et al.[37]). It can be seen that, for any corrosion penetration, the models by Molina et al.[39] and Torres-Acosta and Martínez-Madrid[38] provide the most conservative and unconservative estimates of the crack width, respectively. The model by Andrade et al.[37] explicitly incorporates the influence of the cover-to-bar diameter ratio and of the tensile strength of concrete, in addition to that of the corrosion degree, and has been validated against a homogeneous set of accelerated corrosion tests. This formulation, particularly suitable for generalized corrosion conditions as those treated in this work, is selected in this paper for estimating the corrosion-induced degradation of concrete compressive strength via Equation (10). The corresponding trend of the compressive strength reduction through Equation (10) is illustrated in Figure 3c. The coefficient β_{f_c} could also be applied to reduce the concrete ultimate strain ε_{cu}, in addition to the compressive strength, that is, $\varepsilon_{cu}^* = \beta_{f_c}\varepsilon_{cu}$,[7] so as to produce a simultaneous degradation of strength and ductility in corroded concrete members. This reduction coefficient β_{f_c}, in the original model of Coronelli and Gambarova,[35] was applied uniformly to the entire concrete section. However, it might be reasonable to guess that the corrosion-induced degradation of concrete material properties is more pronounced in the concrete portion close to the corroded bars, rather than in the overall concrete section. This suggest applying Equation (10) selectively, that is, only to the concrete area actually affected by corrosion phenomena, as clarified in the next section.

3 | PROPOSED FIBER HINGE MODEL FOR CORRODED RC ELEMENTS

Let us consider a cantilever RC element (fixed support) having length H and subjected to a constant axial load N and a superimposed cyclic displacement $\delta(t)$, as illustrated in Figure 4 – this is the typical experimental setup for testing RC columns under cyclic loading,[53] including corroded RC columns tested in the literature.[1–6] The cross-section of the RC column has width b_c, height h_c, and is reinforced with steel longitudinal bars having (uncorroded) diameter ϕ and stirrups. The fiber hinge model proposed in this work implies that the column is assumed with linear elastic behavior for a major portion of its length, while plastic deformations remain concentrated over a specified hinge length located at the elements end. This approach is incorporated in the so-called fiber hinge element in SAP2000[54] and can be considered as a hybrid strategy combining the accuracy of distributed-plasticity models with the computational advantages of concentrated-plasticity formulations.

Corrosion-induced degradation of material parameters is implemented at the fiber level in the stress–strain law, depending on the position of the fiber in the cross section. The concrete area in the neighborhood of the corroded steel bars was termed ineffective confined concrete by Di Sarno and Pugliese,[7] as opposed to the effective confined concrete represented by the concrete area farther from the corroded bar. In the fiber-hinge model proposed in this paper, distinct constitutive relationships are adopted in the ineffective and effective confined concrete, concrete cover, and steel bars, cf. again the sketch in Figure 4. Fibers belonging to the concrete cover are described by the Kent and Park model.[55] Fibers belonging to the ineffective confined concrete (delimited by a width 2ϕ toward the internal side of the stirrups) are described by the Mander et al.[56] confinement model. It is assumed that both concrete cover and ineffective confined concrete are affected by corrosion phenomena

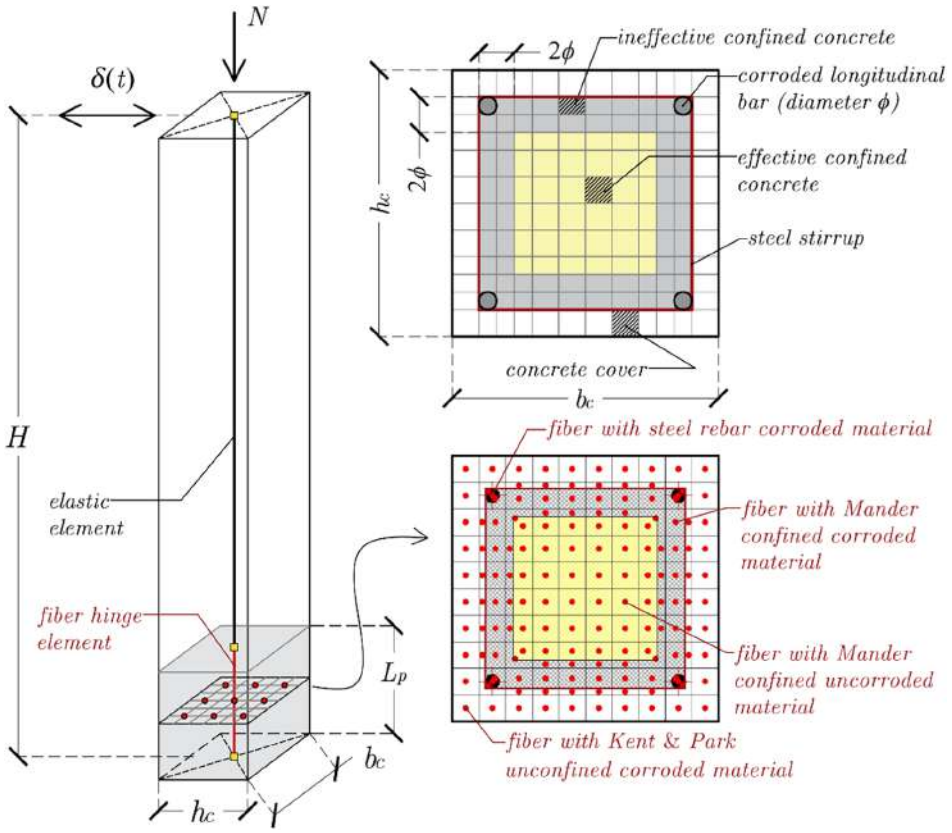

FIGURE 4 Fiber hinge model of corroded RC column and material assumptions for concrete and steel fibers depending on the position of the fiber in the cross section

and, consequently, corrosion-induced reduction of strength and ductility according to the parameter β_{f_c} in Equation (10) is applied in the stress–strain laws of the pertinent fibers. On the contrary, fibers belonging to the effective confined concrete are assumed to be unaffected by corrosion and are described by the Mander et al.[56] confinement model without applying any material property degradation law. This implies that the Coronelli and Gambarova model,[35] that is, Equation (10), is applied selectively to the concrete portions of the cross section. Finally, steel bars are described as fibers by the built-in "rebar" material model of SAP2000,[54] with a stress plateau after the attainment of the yield strength, followed by a curvilinear strain hardening up to the ultimate strength: here, the corrosion-induced reduction of strength and ductility is incorporated according to Equations (6) and (7). The model neglects bond deterioration between concrete and reinforcement, which would reduce the element deformation capacity, and buckling phenomena that may occur in corroded compressed bars (which could be easily incorporated via a tailored, asymmetric in tension and compression, stress–strain law for longitudinal bars, e.g., Refs.33,34). Moreover, the model inherits the limitations of beam-bending formulations that do not incorporate slab action and localized membrane effects in the corners of cross section.

4 | VALIDATION AGAINST EXPERIMENTAL FINDINGS FROM THE LITERATURE

Two cyclic tests on RC columns (one corroded and one uncorroded) whose experimental results were presented by Meda et al.[5] are simulated to assess the capability of the proposed fiber hinge model to describe the cyclic behavior of corroded RC columns, especially the reduction of strength and energy dissipation capability induced by corrosion. In the considered experimental campaign, a preliminary calibration of the artificial corrosion process, through electrolytic cells, was carried out on both bare and embedded bars. The results of this preliminary study offered reliable information on the actual corrosion level of the bars involved in the experimental tests, which is used here in the calibration of the material degradation laws within the fiber hinge model.

By referring to the symbols in Figure 4, the columns tested by Meda et al.[5] have square cross section with $b_c = h_c = 30\,\text{cm}$, height $H = 1.5\,\text{m}$, transverse reinforcement $\phi 8$ mm stirrups @ 30 cm and longitudinal reinforcement represented by four $\phi 16$ mm bars at the section corners (concrete cover 3.5 cm). Steel stirrups of the corroded column were coated by an appropriate protective paint to prevent corrosion; consequently, only the longitudinal bars underwent the artificial corrosion

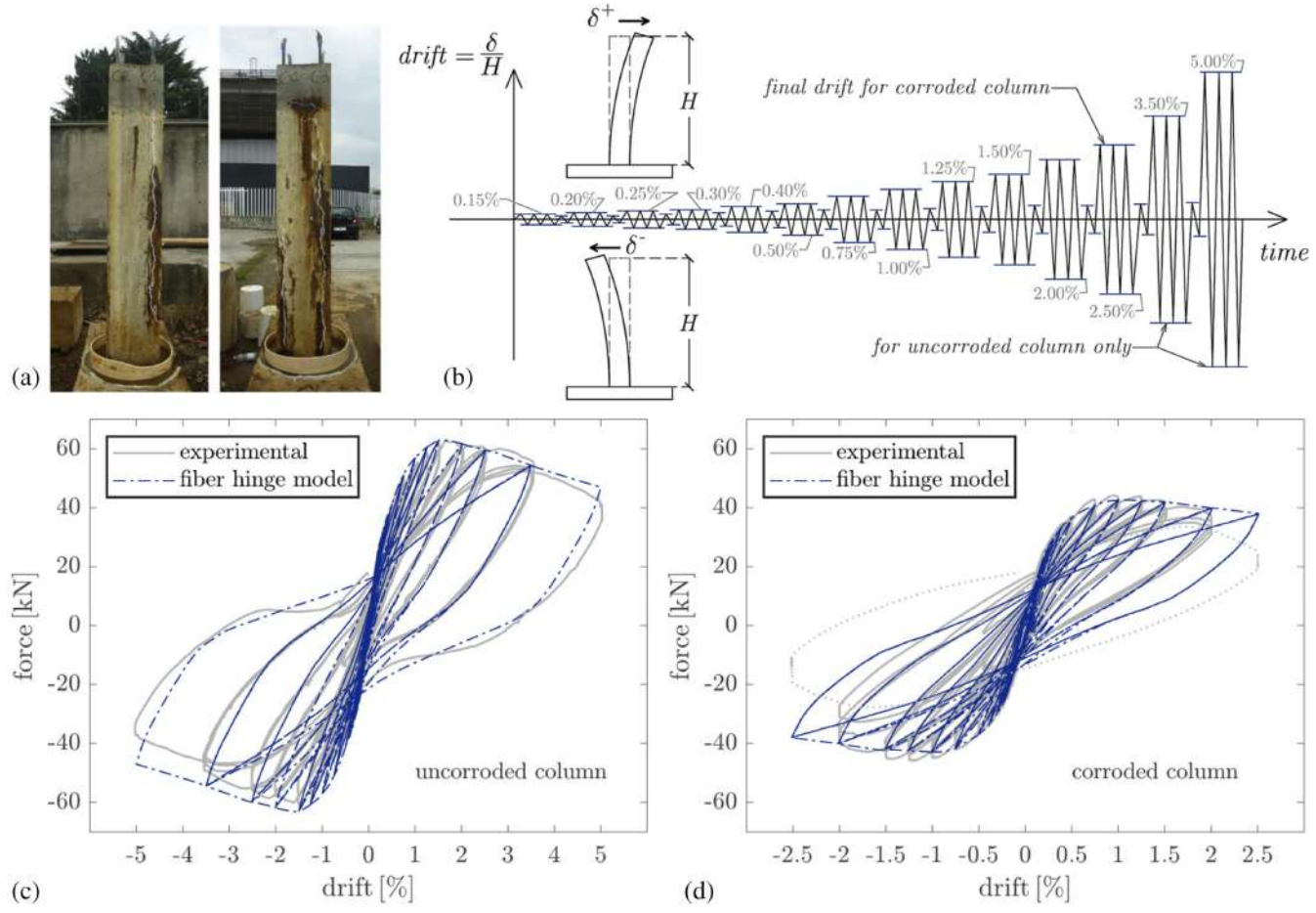

FIGURE 5 Photograph of corroded RC columns tested by Meda et al.[5] (a), time history of imposed drift (b), and comparison between experimental and numerical force-drift cycles (c, d).

process (Figure 5a), with average corrosion degree $\Delta m = 20\%$ (mass losses of 22.6%, 18.7%, 20.6% and 24.1% were measured in the four bars[5]). As to the material properties, the concrete average compressive strength was 20 MPa, while the steel bars had average yield and ultimate strength equal to 520 MPa and 620 MPa, respectively. Considering the above-mentioned material properties, the application of the empirical relationships presented in Section 2 for $\Delta m = 20\%$ led to the stress–strain curves shown in Figure 6 for concrete and steel, which are implemented in the fiber hinge model as explained in the previous section. In particular, $\beta_{f_c} = 0.68$ is assumed in Equation (10) for concrete cover and ineffective confined concrete fibers: this value is obtained from the formulation of Andrade et al.[37] for the crack width w_{cr}. With regard to steel fibers, it is worth mentioning that in the tested RC columns[5] hot-rolled, quenched and self-tempered (QST) reinforcing bars (Tempcore® process) were used, which are characterized by a peculiar annular distribution of the mechanical properties: a low-strength inner ferritic core (with pronounced yield plateau[57]), an intermediate bainitic transition crown and a high-strength martensitic outer anulus (lacking a yield plateau[57]). In this case, the corrosion-induced material degradation is influenced by the inherent heterogeneous (layered) microstructure[25,58]: as an example, for the average mass loss $\Delta m = 20\%$, an idealized residual diameter of 14.3 mm (from the original diameter of 16 mm) is obtained, which implies that approximately 2/3 of the outer martensitic layer would be lost (assuming the transition zone recommended by Haefliger & Kaufmann[57]). Strictly speaking, the overall stress–strain curve of the corroded QST bars should depend on the ratios of areas of residual layers.[57] Nevertheless, for simplicity it has been assumed that corrosion does not affect substantially the shape of the stress–strain law[5,29,32] in terms of elastic modulus (205 GPa) and hardening strain (assumed equal to 2.25%, based on the experimental data from this test campaign[5] and other literature studies[59]): in Figure 6 corroded bars are assumed to exhibit a similar curve to that of uncorroded bars, with a distinct yield plateau and reduced yield and ultimate strength, calculated as per

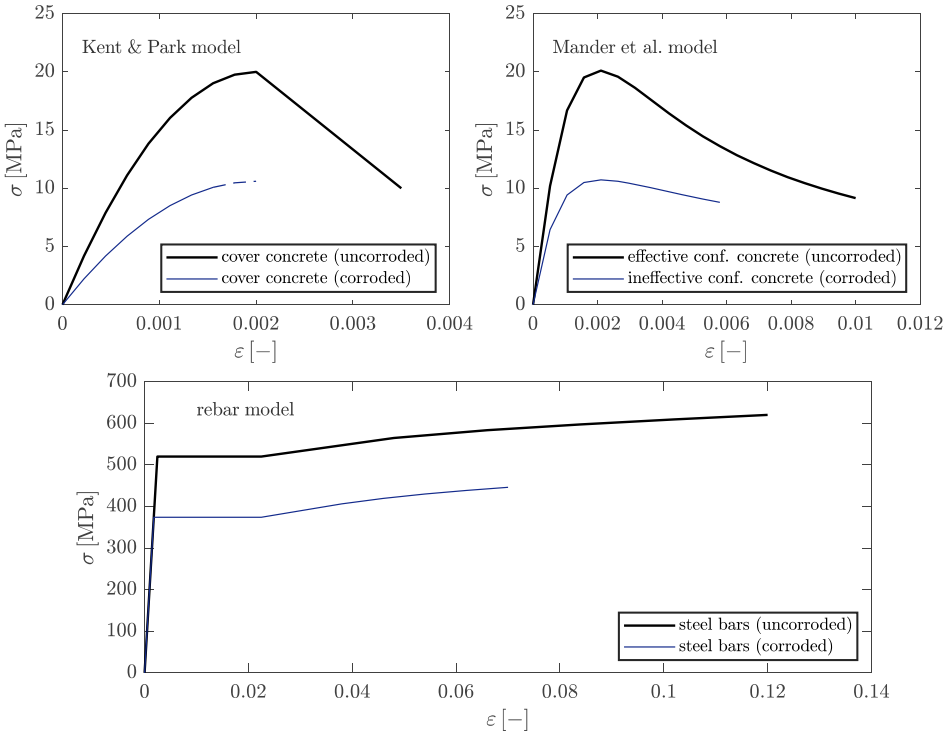

FIGURE 6 Stress–strain relationships for concrete cover (Kent & Park model[55]), confined concrete (Mander et al. model[56]), and steel bars (rebar model[54]) in the uncorroded and corroded RC column tested by Meda et al.[5]

Equation (6) (assuming $\beta_{Fy} = \beta_{F_u} = 0.014$[29]), and reduced ductility, calculated through the second of Equation (7) (assuming $\widehat{\beta}_{\varepsilon_{su}} = 0.0277$[47]). The comparison between the cover constitutive law (unconfined concrete) and the confined concrete stress–strain relationships reveals that the increase of the concrete strength due to the confinement action of stirrups is relatively modest; this result is consistent with the relatively weak transverse reinforcement in the tested columns, which was purposely designed by Meda et al.[5] to be representative of existing Italian structures constructed in the 60–70 s. Takeda and kinematic hysteresis models are adopted for concrete and steel fibers, respectively. The plastic hinge length located at the column base is set equal to the section depth, which is consistent with the considered experimental results[5] as well as with typical values of plastic hinge lengths recommended in design standards and literature works.[60,61] The plastic hinge length may differ for corroded and uncorroded elements, but this issue has not been properly investigated yet.

The RC columns were tested under a constant axial load $N = 400$ kN and a superimposed cyclic displacement. The displacement time history applied to the columns consists of triplets of drifts of increasing amplitude as per ACI Committee 374 guidelines,[53] ranging from 0.15% up to 5.00% for the uncorroded specimen and up 2.50% for the corroded RC column. An intermediate unloading cycle is applied in between two subsequent drift triples, as shown in Figure 5b. These loading conditions are reproduced in the numerical model. Nonlinear Direct Integration History analysis is performed in SAP2000[54] through the Hilber-Hughes-Taylor time integration method.

The numerical results, in terms of force-drift curves, are compared in the bottom part of Figure 5 with the experimental hysteresis loops of the two tested columns. By looking at the uncorroded column (Figure 5c), it can be seen that the prediction is very good not only in terms of backbone, maximum force, and strength degradation during repeated cycles, but also in terms of overall energy dissipation along the entire force-drift cycles. Relevant results are listed in Table 1. The difference in terms of maximum force is almost null (relative error of 0.16%), while the differences in terms of energy dissipation are around 3.7%. With regard to the corroded column (Figure 5d) in general a reasonably good predictive performance is observed in terms of backbone, maximum force and strength degradation over repeated cycles. The discrepancies between experimental and numerical results are in the range of 6% in terms of both maximum force and energy dissipation. By looking at the loading and unloading stiffness, except for the last cycles at 2.50% drift level that correspond to a very damaged scenario of the corroded column, all the other cycles are captured relatively well by the numerical model.

The results obtained from the fiber hinge model are consistent with experimental findings. It is worth noting that, once appropriate degradation laws to account for corrosion effects at the material level are defined (as overviewed in Section 2), the proposed fiber-hinge model does not require any further ad-hoc calibration of the moment-curvature relationship and, consequently,

TABLE 1 Force and energy dissipated obtained by numerical model compared with experimental results

	Maximum force (kN)			Energy dissipated (kJ)		
Specimen	**Experimental**	**Numerical**	**Relative error (%)**	**Experimental**	**Numerical**	**Relative error (%)**
Uncorroded	63.00	63.1	0.16	27.85	28.88	3.69
Corroded	45.76	42.91	6.24	13.88	13.05	6.03

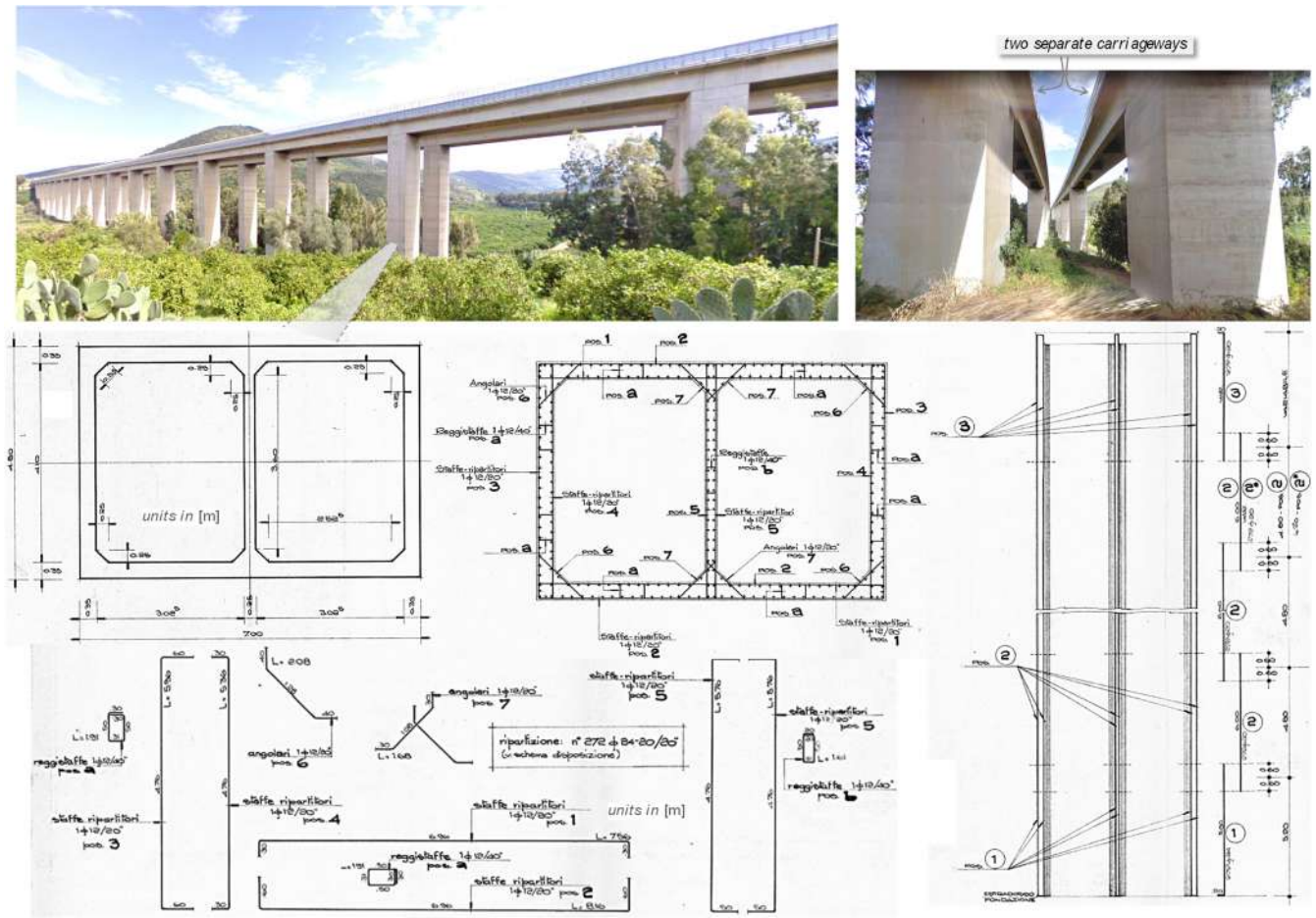

FIGURE 7 Photographs of the Zappulla viaduct (Sicily, Italy) (top) and reinforcement arrangement from original drawings (bottom)

lends itself to be applied to other cross-section shapes and complex reinforcement layouts. To prove these potentials, in the next section the model will be utilized to perform the seismic vulnerability assessment of the Zappulla multi-span viaduct whose RC piers, with box-shaped, two-cell hollow rectangular cross section, are characterized by a widespread corrosion state.

5 | THE CASE STUDY OF THE ZAPPULLA VIADUCT

Belonging to the A20 highway Messina-Palermo, the Zappulla viaduct is located in the municipality of Rocca di Capri Leone (Sicily, Italy), at around 2 km from the Tyrrhenian Sea. Built in the first 1970s, it consists of two separate carriageways for the two traffic directions (one from Messina to Palermo and the other in the opposite direction), has 18 spans of 45.4 m length, thus extending for around 820 m. The superstructure is composed of two U-shaped prestressed concrete girders mutually collaborating through transverse diaphragms (two near the supports and three along the span) and an overlying RC slab. In the longitudinal direction, the girders are simply supported on neoprene bearings according to a statically determinate scheme[62]; in the transverse direction, RC seismic devices (four per pier, monolithically connected to the pier caps and to the abutments) restrain the transverse movements of the deck.

FIGURE 8 Widespread corrosion state on the RC piers of the Zappulla viaduct detected from visual inspection

As shown in Figure 7, each carriageway has a rectilinear route and includes two abutments and 17 piers of variable height from 17 to 47 m. All the piers have a box-shaped, two-cell hollow rectangular cross section with plan dimensions 7.00 × 4.80 m and are reinforced with 272 longitudinal bars, which are ϕ24 mm for the first 5 m from the foundation, and ϕ20 mm for the rest of the pier height. From the design drawings, transverse reinforcement represented by ϕ12 mm stirrups @ 20 cm, angular bars ϕ12 mm @ 20 cm (placed in the corners of the section) and brackets ϕ12 mm @ 40 cm spacing (to reduce the free length of the stirrups in the longer sides) are present, as depicted in Figure 7. With regard to the materials, the original drawings report concrete type IV (generally, cube characteristic strength ≥25 MPa), and high elastic limit steel ("acciaio ad alto limite elastico – ALE" in Italian) whose presumed (median) yield strength is 500 MPa, based on 461 test certificates collected for steel lots produced in a period (1950–1980) consistent with that of the bridge construction.[63]

5.1 | Visual inspection and defect detection

With its 50 years of service life (built in the first 1970s, open to traffic some years later in 1977), the safety conditions of the Zappulla viaduct are strongly affected by carbonation and chloride-induced corrosion observed in its piers. As depicted in Figure 8, damping stains are visible along the RC piers, along with diffuse micro-cracking, in some cases accompanied by total detachment of concrete cover. In the areas affected by cover detachment (more frequently observed near the pier base), reinforcing bars and stirrups exhibit a high degree of corrosion, which results in a reduction of resistant area as well as strength

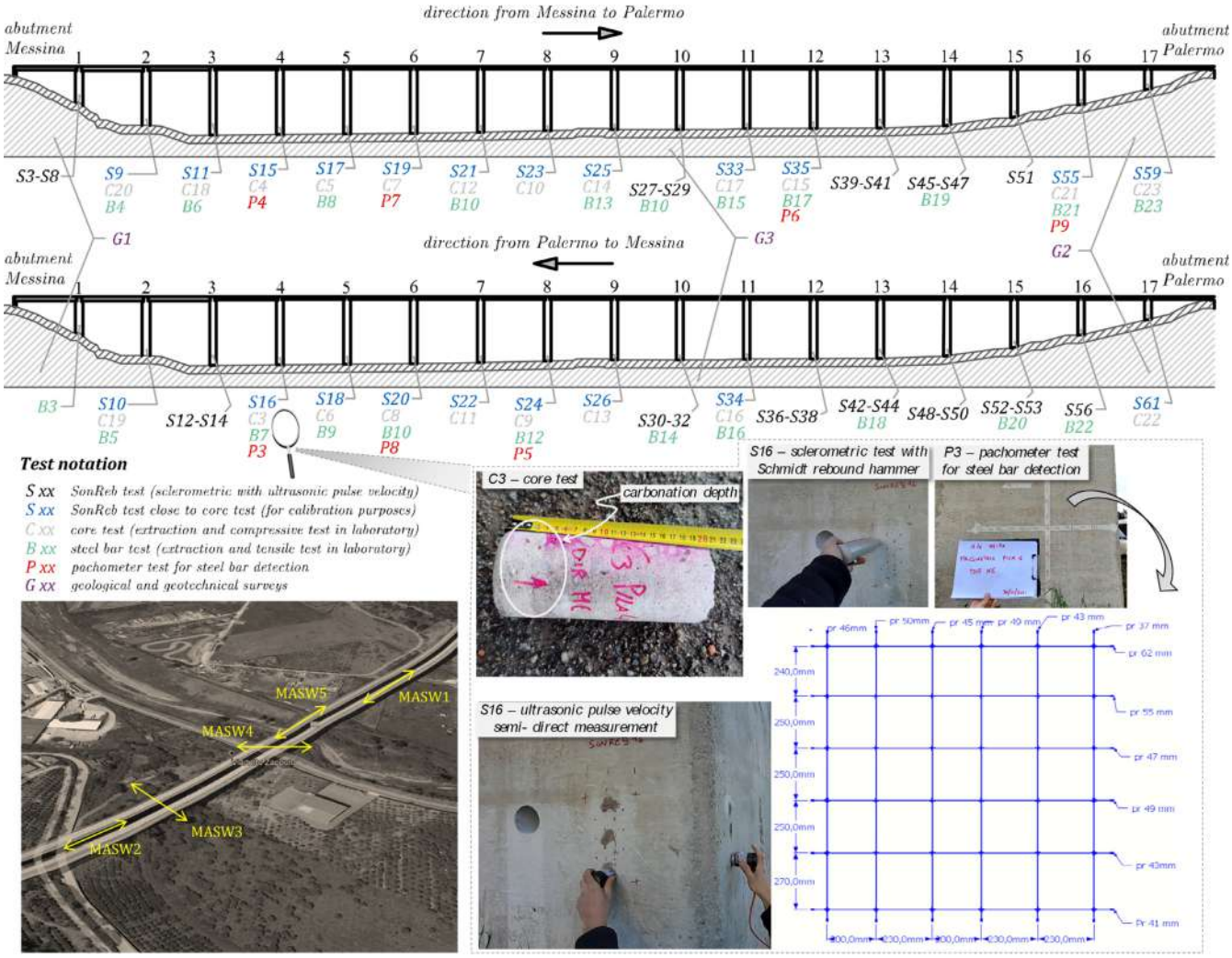

FIGURE 9 Designation and location of experimental tests performed on the Zappulla viaduct

and ductility characteristics. At higher altitudes of the piers, exposure to corrosive agents coming from the surrounding marine environment caused the deterioration of the cortical part of concrete, where medium-size cracks can be observed, especially on the sides facing the sea. Also in this case, the phenomenon of concrete carbonation contributed to the oxidation of longitudinal and transverse bars. Although a restoration intervention was attempted some years ago, it was not effective because the repairing mortar was unable to develop the necessary grip with the underlying deteriorated layer.

5.2 | Experimental campaign for material parameters determination

Considering the deterioration state identified from visual inspection, a comprehensive in-situ testing campaign was planned and executed. Designation and position of experimental tests are illustrated in Figure 9. First, geological, geotechnical and geophysical surveys were conducted to characterize the soil characteristics, including three mechanical rotating boreholes and continuous core drilling up to 40 m of depth (G1-G3 in Figure 9), 10 standard penetration tests (SPT) and five multichannel analysis of surface waves tests (MASW1-MASW5) with lines of 56.0 m to compute the $v_{s,30}$. It was found that the interested soil comprises slightly silty sand (depth 0–4 m), gravel (4–6.5 m) and fractured greenish gray phyllades (>6.5 m). SPT values (Nspt) ranging from 45 to 97 and $v_{s,30}$ ranging from 380 m/s to 700 m/s led to the identification of ground type B as per Table 3.1 of Eurocode 8-Part 1 (EC8-1).[61]

Subsequently, the experimental campaign on the 17 + 17 RC piers along the two carriageways comprised: (1) concrete coring (extraction and compressive tests in laboratory) in 21 piers (C3-C23); (2) steel bar characterization (extraction and tensile tests in laboratory) in

21 piers (B3-B23); (3) combined sonic and rebound (SonReb) tests in 59 different locations (S3-S61), of which 21 close to the core tests for calibration purposes; (4) pachometer tests for steel bar detection in seven different piers (P3-P9); (5) measurements of corrosion potential with respect to saturated $Cu/CuSO_4$ (copper/copper sulfate—CSE) reference electrode in 41 different locations (CP3-CP43)—not indicated in Figure 9 but discussed in the following subsection 5.3.

The concrete cores were extracted near the bottom part of the piers; after the extraction, upper and lower surfaces were cut (height-to-diameter ratio $h/\phi = 1$), rectified and tested in laboratory to obtain the core compressive strength f_{core}, from which the cube strength R_c was calculated as [Equation (11)]:

$$R_c = f_{core} \times F_d \times c_{dir} \tag{11}$$

where F_d is a disturbance factor computed as per NTC2018,[64] while c_{dir} is a directional factor depending on the extraction mode (in this case set equal to 1.05 for cores extracted perpendicular to the casting direction as per Concrete Society[65] provisions). Core test results are listed in Table 2 for 21 cores (C3-C23) whose location was already shown in Figure 9. The cube strength identified from the tests ranged from 25 MPa to 55 MPa, with a mean value of 37.2 MPa, a mode equal to 29.1 MPa and a coefficient of variation (CoV) of around 20%. In Table 2, the carbonation depth (identified after spraying a phenolphthalein indicator on the extracted cores) is also reported, which will be useful for the critical discussion on the corrosion state in the following subsection 5.3.

In addition to core drilling, SonReb tests were also executed as a nondestructive and cheaper testing technique to obtain a broader range of concrete strength data that can be useful for statistical processing. SonReb tests provide the Schmidt hammer rebound index I_r from sclerometric tests (obtained as average of 12 measurements in spots close to each other as per UNI EN 12504-2:2001) combined with the ultrasonic propagation velocity V_{us} (obtained as average of six measures in spots close to each other as per UNI EN 12504-4:2005). The

TABLE 2 Experimental results from concrete coring on RC piers of the Zappulla viaduct and corresponding SonReb tests utilized for calibration of nonlinear regression coefficients a, b, c

Core ID	Unit weight (kg/m^3)	Core strength f_{core}(MPa)	Cube strength R_c(MPa)[a]	Carbonation depth (mm)	SonReb ID	$V_{us}[m/s]$	I_r[–]
C3	2296.6	28.4	32.2	40	S16	4346.7	34
C4	2342.7	25.7	29.1	40	S15	3937.5	36
C5	2291.5	35	38.2	40	S17	4225.7	32
C6	2370.1	52.7	55.3	10	S18	4202.7	34
C7	2370.5	23	26.3	30	S19	4213.1	35
C8	2256.4	26.1	29.6	30	S20	4040.6	32
C9	2384.5	40.8	42.8	53	S24	4079.5	37
C10	2413.3	42.7	44.8	45	S23	3519.4	34
C11	2374.4	45	47.3	52	S22	4581.7	38
C12	2366.5	36.6	40.0	40	S21	4581.7	37
C13	2385.4	36.9	40.3	50	S26	4596.6	30
C14	2377.8	38.2	41.7	45	S25	3799.9	38
C15	2356.9	32.4	36.1	12	S35	4093.2	30
C16	2357.1	31.5	35.1	50	S34	4093.2	36
C17	2344.5	36.5	39.9	50	S33	4380.6	36
C18	2338	22	25.2	42	S11	3989.3	32
C19	2364.2	29.6	33.6	50	S10	3855	34
C20	2331.4	35.8	39.1	50	S9	4349.2	34
C21	2308.2	27.6	31.3	60	S55	4204.8	36
C22	2369.4	42.9	45.0	15	S61	4371.6	36
C23	2285.4	25.7	29.1	78	S59	3326.3	34

[a]Value calculated in accordance with NTC2018[64] and Concrete Society.[65]

TABLE 3 Nonlinear regression coefficients a, b, c for Equation (12) (V_{us} in [m/s] units, R_c in [MPa] units)

	SonReb correlation coefficients			Normalized square error
Formulation	***a***	***b***	***c***	ε^2
RILEM NDT4 (1993)[79]	9.27×10^{-11}	2.6	1.4	1.0474
Gašparik (1992)[80]	8.06×10^{-8}	1.85	1.246	0.8939
Di Leo & Pascale (1994)[81]	1.2×10^{-9}	2.446	1.058	0.9817
average SR strength	–	–	–	0.9322
NLSQF (this paper)	2.716×10^{-3}	0.81168	0.76265	0.6181

parameters I_r and V_{us} are somehow related to the degree of uniformity and compactness of concrete,[66] to the density and dynamic modulus of the material, and can be useful to identify possible defects or internal cracking.

The values I_r and V_{us} are used to indirectly estimate the compressive strength, for example, the cube strength R_c. In the literature,[67] several empirical correlations were proposed resorting, in most cases, to a power law relationship:

$$R_c = a \times V_{us}^b \times I_r^c \tag{12}$$

where a,b,c represent three regression coefficients. The values of these coefficients for three popular formulations from the literature are listed in Table 3. It can be seen that these coefficients [and the resulting predictions of R_c via Equation (12)] may change from one formulation to the other, since their validity relies upon the database used for their calibration. For this reason, the so-called "average SR strength" is also calculated as the average cube strength resulting from the three considered formulations proposed in the literature, meant as a compromise among different calibrating datasets. In the experimental campaign, 21 out of the total 59 SonReb tests were purposely performed close to core tests for calibration purposes, whose results are listed in the right columns of Table 2 besides the pertinent core test. For these 21 calibrating tests, a nonlinear least-square fitting (NLSQF) procedure is used to determine the most appropriate regression coefficients a,b,c by minimizing the normalized square error:

$$\min_{a,b,c} \varepsilon^2 = \sum_i \left(\frac{R_{c,i}^{exp} - R_{c,i}^{est}(a,b,c)}{R_{c,i}^{exp}} \right)^2 \tag{13}$$

The triplet a,b,c identified from NLSQF is the best, in statistical sense, among all possible combinations complying with Equation (12), as shown by the normalized square error ε^2 value comparatively reported in Table 3 for all the discussed formulations. In particular, a value of ε^2 30%–40% lower than the other formulations is obtained.

Figure 10a reports the identified nonlinear regression surface against the 21 experimental data. Since the parameters Figure 10b,c identified from NLSQF are close to the unity, an almost planar surface can be observed in the relatively limited range of variation of I_r and V_{us} obtained from the experimental campaign. As shown in Figure 10b in all but two cases the core/SonReb strength ratios for the proposed formulation lie within the interval (0.8–1.2), which confirms the effectiveness of the calibration. A clear improvement of the predictive capability of the proposed formula over the average SR strength (literature formulations) is noted. Once the coefficients a,b,c are calibrated, Equation (12) is applied to the remaining 38 SonReb results (i.e., the set of SonReb data not used in the calibration process) to predict the cube strength: Figure 10c depicts the results obtained with the proposed formulation versus those pertinent to the average SR strength (literature formulations). Error bars, denoting the maximum interval of variation (min-max among the three literature formulations), can be meant as a measure of epistemic uncertainty. The area enclosed by the two trends (called "discrepancy area" in the plot) could be interpreted as a measure of error inherent to available literature formulae in predicting reliable strength data without a proper calibration of their empirical coefficients.

Probability distributing fitting is performed to compute statistically meaningful parameters based on the discrete concrete cube strength data resulting from cores (21) and SonReb tests (38). A lognormal distribution is fitted to the data in Figure 11. By minimizing the negative loglikelihood function, the best-fit parameters of the fitting lognormal distribution are $\mu_{logR} = 3.3987$ and $\sigma_{logR} = 0.18027$, from which the identified mean and characteristic (5% fractile) cube strengths are $R_{cm} = 30.41$ MPa and $R_{ck,5\%} = 22.25$ MPa, respectively (CoV = 18.1%, in line with conventional values suggested by the fib Bulletin 80[68] for existing structures).

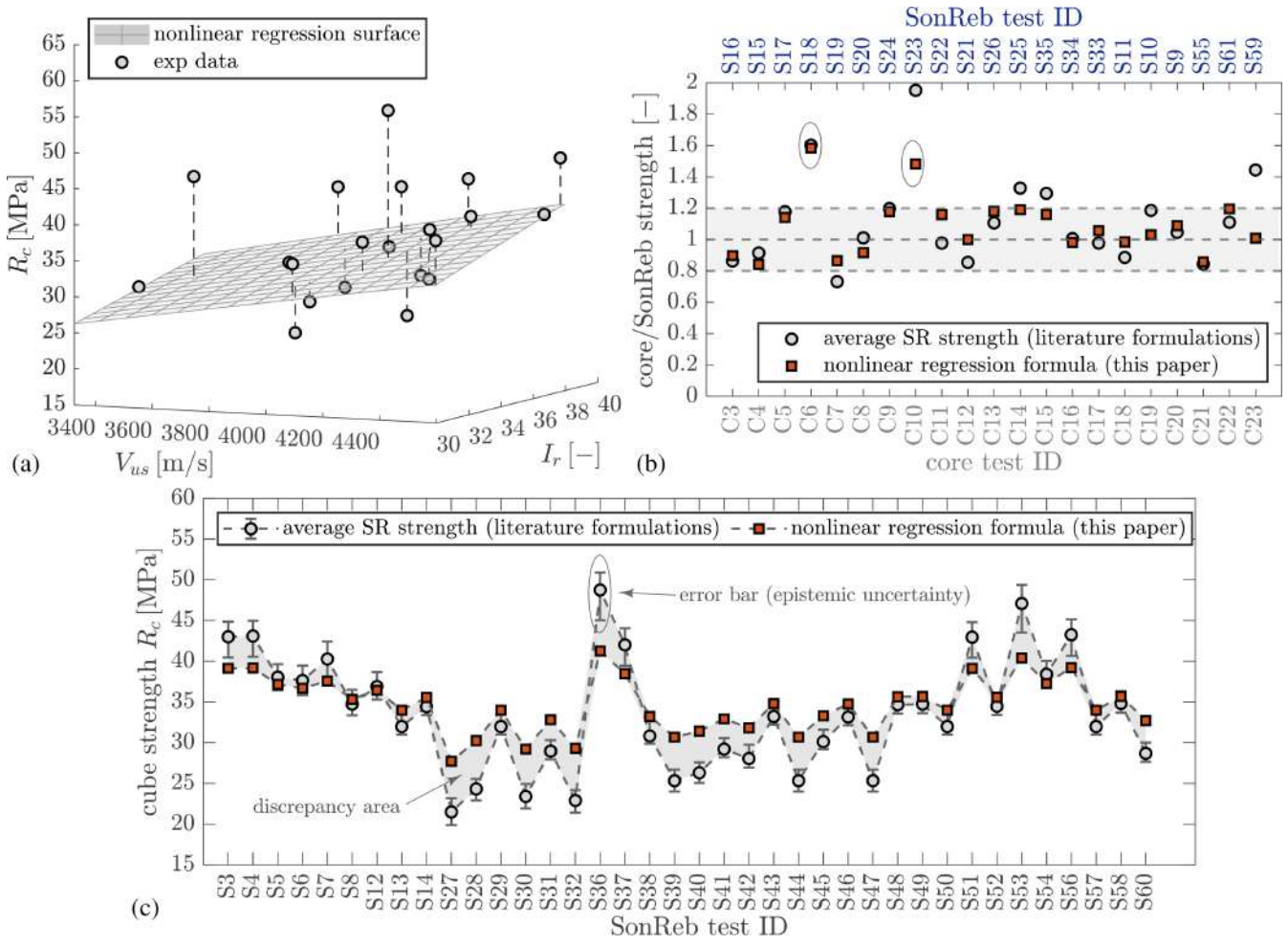

FIGURE 10 Determination of concrete compressive strength through SonReb tests calibrated based on core tests

With regard to steel reinforcement characterization, 21 bars were extracted from the piers and tested in laboratory to obtain the tensile yield and ultimate stress, f_y and f_u, respectively, and the ultimate strain ε_{su}. The experimental mechanical parameters of each extracted bar (f_y, f_u, ε_{su}) were retrieved from archives of testing certificates made available by the road management body, have been statistically processed, and are listed in Table 4 (mean and CoV). Unfortunately, the original stress–strain curves of the tested bars were not found in such archives, thus only idealized relationships can be derived, on the basis of typical constitutive equations of hot-rolled carbon steels—see Figure 13.[69] Although the actual $\sigma - \varepsilon$ curves of the extracted bars might be slightly different from those postulated in Figure 13 (e.g., in terms yield plateau length and strain hardening branch), these curves reflect the values of experimental yield stress, ultimate stress and ultimate strain collected from the testing certificates, which constitute the most relevant parameters for the seismic vulnerability assessment of the RC piers. It was noted that four of the bars extracted from the transverse reinforcement of the piers (stirrups), more exposed to the cortical part of the section than longitudinal reinforcement, had reduced area compared to nominal diameter ϕ12 mm (i.e., they exhibited mass loss), which was indicative of an undergoing corrosion process. These test results will be further discussed in the following subsection 5.3.

Finally, pachometer tests revealed that stirrup spacings were larger than expected from design drawings (i.e., 20 cm). In particular, the detected spacing ranged from 19 cm to 38 cm, with a mean value of 27 cm (CoV 16.6%). This is a crucial aspect in quantifying the confinement action of transverse reinforcement and will be taken into account in the following numerical analyses.

5.3 | Critical considerations on the corrosion state

By measuring the potential between a metallic part (laid bare after removing a small part of section cover) and the

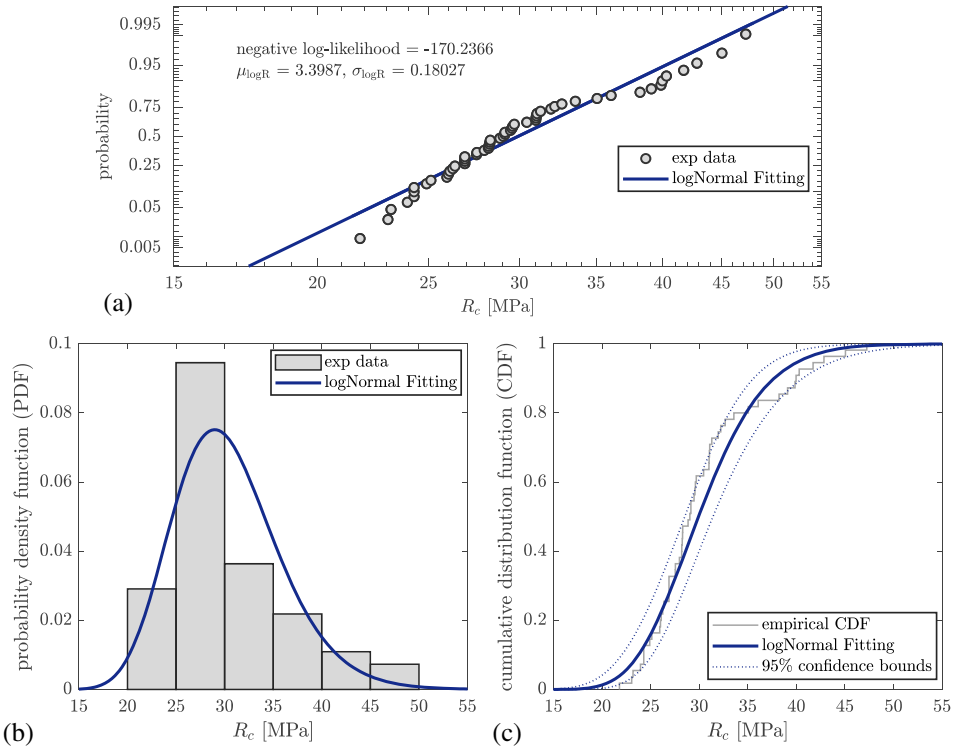

FIGURE 11 Lognormal distribution fitting of concrete compressive strength based on core tests and SonReb tests

TABLE 4 Mechanical characteristics of steel bars extracted from RC bridge piers and tested in laboratory

ϕ (mm)	N. Bars	Actual diameter (mm) Mean (CoV)	f_y (MPa) Mean (CoV)	f_u (MPa) Mean (CoV)	ε_{su} (%) Mean (CoV)
20	3	20.1 (0.97%)	429.5 (3.42%)	667.1 (2.19%)	12.9 (4.26%)
24	8	24.0 (0.65%)	423.1 (2.74%)	678.3 (3.58%)	11.9 (9.35%)
12	6	12.1 (2.46%)	446.9 (7.13%)	671.4 (4.60%)	13.1 (6.46%)
12[a]	4	**10.2 (8.66%)**	412.8 (5.59%)	630.0 (3.55%)	12.0 (13.69%)

[a]Values in corroded bars with reduced area (i.e., exhibiting mass loss) compared to nominal diameter ϕ12 mm (see subsection 5.3).

surrounding concrete, it is possible to identify actively corroding steel bars embedded in reinforced concrete structures as the most negative areas in a potential field.[70] The system consists of a high-sensitivity voltmeter and a saturated reference electrode (standard half-cell[71]); these tests are performed in compliance with UNI 10174:1993 standards.

The results are expressed in the form of a chromatic map (potential mapping with equi-potential contour plots) representative of the potential measured on the investigated area (Figure 12). Since each corrosion condition is typically associated with specific intervals of the corrosion potential, the potential difference may be symptomatic of ongoing (localized or generalized) corrosive phenomena. For carbon steel bars, typical ranges reported in Appendix X1 of ASTM C876-91[72] are as follows: potentials higher than −200 mV with respect to the CSE saturated reference electrode can be associated with a low-to-very low probability of corrosion (<10%); potentials lower than −350 mV are generally pertinent to high probability of corrosion (>90%); intermediate potentials $-200\,\text{mV} < p < -350\,\text{mV}$ can be representative of medium-high probability of corrosion but, in general, corrosion activity is deemed uncertain. Min, max, mean, and standard deviation (std) values recorded in the 41 corrosion potential maps are listed in Table 5: it is evident that most of the piers would be exposed to a medium-high / high probability of corrosion according to ASTM C876-91 recommendations.[72] Values marked in bold in Table 5 are pertinent to the four potential maps shown in Figure 12. The above-mentioned intervals suggested by ASTM C876-91[72] should be treated with caution as they were empirically derived from a specific situation (chloride-induced corrosion of cast-in-place bridge decks in the USA) that cannot be considered universally applicable. In reality, the ASTM C876-91[72] criteria can only give a rough guidance in the interpretation of the potential mapping unless a case-specific statistical treatment of the

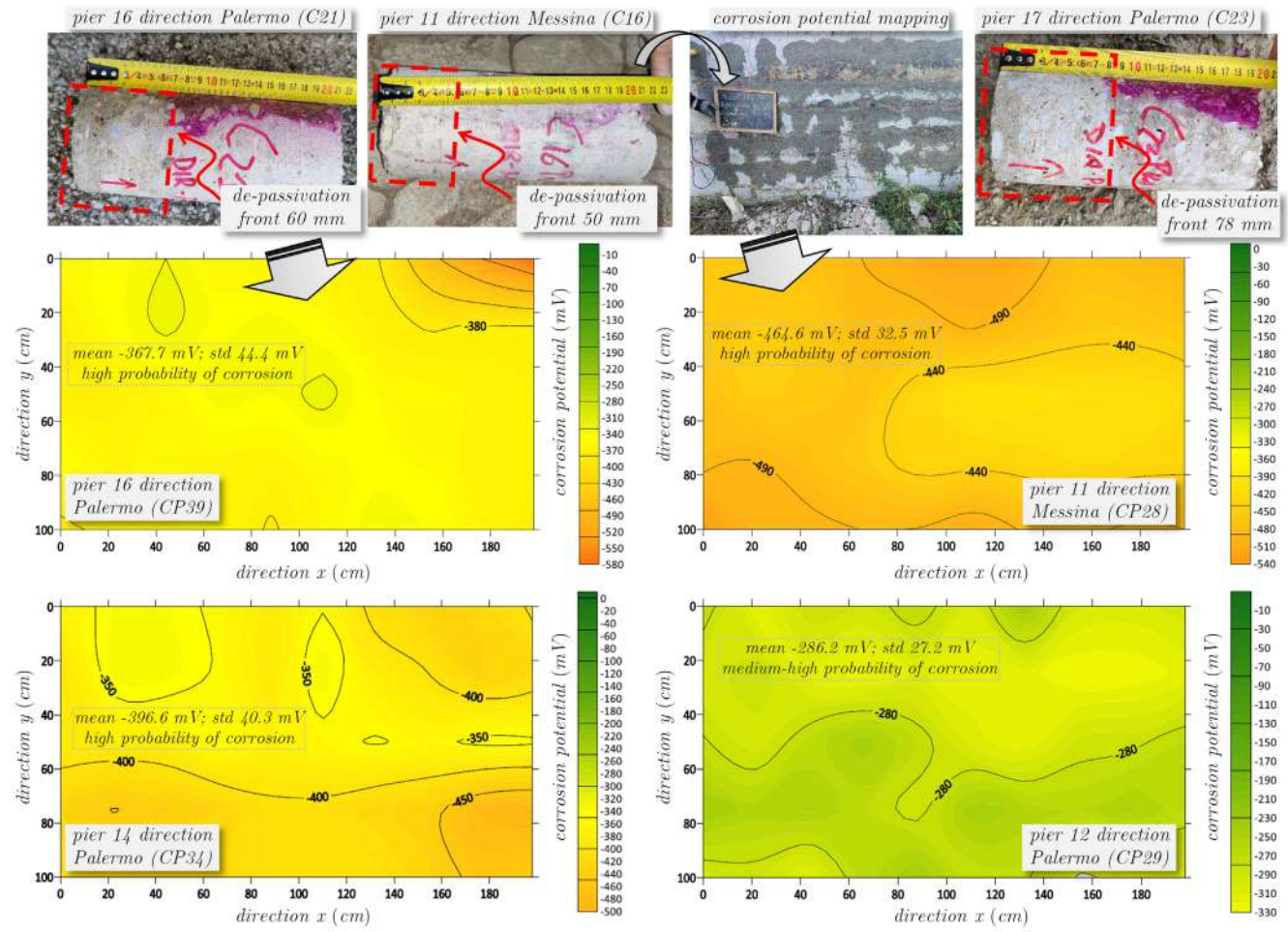

FIGURE 12 Identification of corrosion through carbonation tests and maps of corrosion potential

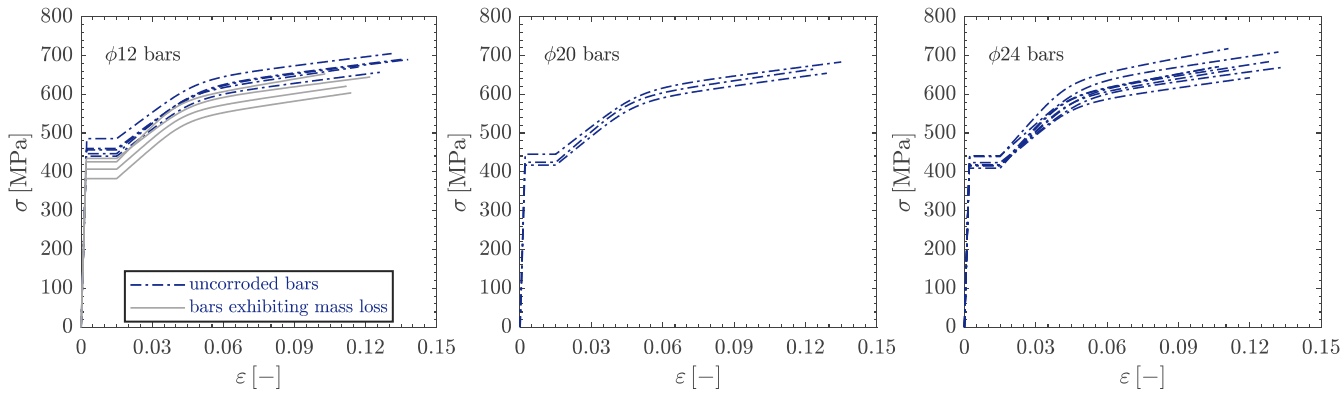

FIGURE 13 Stress–strain curves of steel bars extracted from RC piers (data in the plots are critically derived by the authors based on experimental values of yield strength, ultimate strength, and ultimate strain collected from the testing certificates)

half-cell potential measurements is preliminarily performed.[70,71] Aware of the limitations of the intervals given in the ASTM C876-91,[72] in this work potential mapping was used as a qualitative test method, whose results were interpreted critically with the aid of other tests (carbonation tests, environmental exposure conditions, tensile tests of extracted steel bars) performed in the same investigated areas. As an example, half-cell potential measurements replicated onto two faces of the same pier (e.g., CP20 and CP21 in pier 8 direction

TABLE 5 Experimental results from maps of corrosion potential with respect to saturated CSE reference electrode on RC piers of the Zappulla viaduct and estimate of probability of corrosion

		Corrosion potential with respect to saturated CSE reference electrode				
Test ID	**Pier (dir.)**	**Min (mV)**	**Max (mV)**	**Mean (mV)**	**Std (mV)**	**Prob. of corrosion**
CP3	1 (Pa)[a]	9	143	84.1	39.8	L
CP4	1 (Pa)[b]	10	118	53.4	30.3	L
CP5	1 (Me)	67	190	162.3	20	L
CP6	2 (Pa)	−275	−206	−234.9	14.9	MH
CP7	2 (Me)	−333	−260	−292.2	13.1	MH
CP8	3 (Pa)	−267	−130	−214.1	30.4	MH
CP9	3 (Me)	−274	−12	−88.8	61.1	L-MH
CP10	4 (Pa)[a]	−290	−107	−219.9	41.3	L-MH
CP11	4 (Pa)[b]	−261	−125	−192	29.1	L-MH
CP12	4 (Me)	−154	−50	−122.9	18.8	L
CP13	5 (Pa)	−162	−4	−62.2	35.8	L
CP14	5 (Me)	−483	−276	−392.6	42.1	H
CP15	6 (Pa)[a]	−577	−343	−469.1	48.3	H
CP16	6 (Pa)[b]	−241	−112	−184.8	28.6	L-MH
CP17	6 (Me)	−655	−301	−370.5	46.2	MH-H
CP18	7 (Pa)	−484	−302	−394.2	43.4	MH-H
CP19	7 (Me)	−618	−456	−525.3	30.7	H
CP20	8 (Pa)[a]	−764	−507	−651.8	41.7	H
CP21	8 (Pa)[b]	−510	−338	−409.4	36.5	MH
CP22	8 (Me)	−254	−51	−159.2	48.4	L-MH
CP23	9 (Pa)	−238	−46	−147.8	55.6	L-MH
CP24	9 (Me)	−336	−236	−284.5	24.6	MH
CP25	10 (Pa)	−527	−355	−433.6	42.8	H
CP26	10 (Me)	−257	−142	−198.8	32.2	L-MH
CP27	11 (Pa)	−389	−128	−242	54.9	L-MH
CP28	**11 (Me)**	**−537**	**−403**	**−464.6**	**32.5**	**H**
CP29	**12 (Pa)**	**−333**	**−239**	**−286.2**	**27.2**	**MH**
CP30	12 (Me)	−400	−133	−237.8	85.4	MH
CP31	13 (Pa)[a]	−420	−105	−278.8	81.3	MH
CP32	13 (Pa)[b]	−269	−143	−222.1	32.6	MH
CP33	13 (Me)	−283	−19	−228.1	43.6	MH
CP34	**14 (Pa)**	**−492**	**−331**	**−396.5**	**40.3**	**H**
CP35	14 (Me)	−423	−145	−284.7	68.2	MH
CP36	15 (Pa)[a]	−520	−250	−371.9	73.6	MH-H
CP37	15 (Pa)[b]	−350	−44	−175.4	59	L-MH
CP38	15 (Me)	−132	−2	−48.8	32.8	L
CP39	**16 (Pa)[a]**	**−576**	**−323**	**−367.7**	**44.4**	**H**
CP40	16 (Pa)[b]	−175	−12	−74.1	33.9	L
CP41	17 (Pa)	−259	−189	−227.7	17.4	MH-H
CP42	17 (Me)[a]	−248	−31	−124.9	63.3	L-MH
CP43	17 (Me)[b]	−246	−4	−72.6	51.9	L

Abbreviations: H, high (< −350 mV); L, low (>200 mV); MH, medium-high.

[a]face exposed to the sea.

[b]face opposite to the sea.

Palermo) revealed that potentials values were reasonably lower (corresponding to a higher probability of corrosion) in faces exposed to the sea (in which corrosion is reasonably more pronounced) than in faces of the same pier opposite to the sea. Furthermore, it was noted that piers with lower potentials values were also those with larger de-passivation fronts detected from the carbonation tests (see e.g., results for pier 11 direction Messina in Figure 12). Finally, it was possible to extract some representative specimens of steel bars from piers 12, 14 direction Palermo and from pier 11 direction Messina (whose potential maps are shown in Figure 12), as well as from pier 17 direction Palermo (whose carbonation depth is illustrated in Figure 12). Bars extracted from these piers were characterized by diameters lower than 12 mm, with mass losses ranging from 12.1% up to 42.1% (diameters from 9.13 mm to 11.25 mm). The corresponding yielding and ultimate load strengths of these four steel specimens are depicted in Figure 14 in terms of F_y^*/F_y and F_u^*/F_u ratios (the values F_y and F_u of the uncorroded bars were taken as the mean values for the ϕ12 mm bars listed in Table 4). As an example, for the steel bar extracted from pier 17 (B23 test) with $\Delta m = 42.1\%$, the reduction of yielding and ultimate strength detected from experimental tensile tests in laboratory was of around 50% compared to the uncorroded bar. This pier was also characterized by the largest de-passivation front (of almost 80 mm, cf. again Figure 12) among the extracted cores listed in Table 2. Similarly, for the steel bar extracted from pier 14 (B19 test) with $\Delta m = 31.5\%$, which was characterized by high probability of corrosion according to the corrosion maps CP34 in Figure 12, experimental values of F_y^*/F_y and F_u^*/F_u from tensile tests were around 0.65. It can be noted that experimental data concerning yielding load and ultimate load degradation of corroded steel bars are well described by the linear decaying relationships of Equation (6), with β_{F_y} and β_{F_u} in the range 0.012–0.014, in accordance with other literature studies.[7] This demonstrates that the confinement action exerted by stirrups in the RC piers may be significantly affected by corrosion. However, as noted in the next subsection, confinement of the piers of the Zappulla viaduct is already very low regardless of corrosion-induced degradation of stirrups, because of the large distance of brackets and the large spacing of transverse reinforcement.

It can be concluded that a widespread corrosion state was found in the RC piers of the Zappulla viaduct, which is due to both carbonation and chloride contamination along with exiguous cover thickness. Based on the visual inspection, no pitting corrosion nor damage localization was observed in any bar; instead, the oxidation process was found to be uniformly distributed on the whole surface of steel in the exposed reinforcing bars (see again Figure 8) as well as in the extracted steel samples. It is reasonable to think that carbon dioxide present in the moist environment of the Zappulla viaduct (relative humidity between 60% and 90%–95%, depending on seasonal and daily fluctuations of the marine context, corresponding to high carbonation rates[70]) has largely neutralized the alkalinity not only of concrete cover but also, in some cases, of the underlying concrete layers (extensive carbonation). This hypothesis is confirmed by the high values of carbonation depths listed in Table 2, ranging from 30 up to 80 mm, thus even exceeding the cover thickness (20 mm for external stirrups, 30–35 cm for longitudinal bars, based on design drawings). The state of uniform corrosion is also documented by the potential mapping results: the potential values are variable from −250 to −500 mV CSE, which corresponds to a range that is usually well correlated with general corrosion in carbonated concrete.[70] Moreover, the gradient between corroding and passive zones is very important to interpret the nature of corrosion[73]: the potential values measured over the investigated areas vary smoothly, as

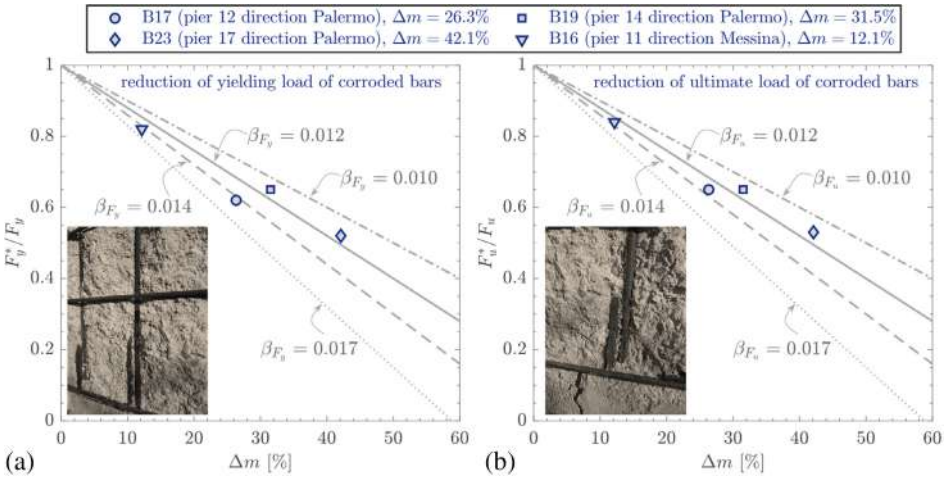

FIGURE 14 Experimental results of yielding load (a) and ultimate load (b) degradation of corroded steel bars extracted from RC piers

confirmed by the representative potential maps in Figure 12 as well as the relatively low values of std [mV] listed in Table 5. These results suggest that the entire surface of reinforcing bar is likely active; instead, pitting corrosion would be typically characterized by abrupt variations in the potential values and high gradients in the corresponding mapping,[70,73] which are nowhere observed in the examined piers.

These considerations (visual inspection, carbonation test results, potential mapping interpretation) has led the authors to assume that the entire surface of reinforcing bars is active, that is, lacking the protective layer (passive film) and, thus, affected by generalized corrosion. Although carbonation was deemed the major source of corrosion, chloride ions penetration from the external environment might be a concomitant factor, triggered by the marine aerosols (the Zappulla viaduct is only 2 km far from the Tyrrhenian Sea). Experimental measurements of chloride content profiles, not available yet, could be certainly useful to confirm this hypothesis. In situations of carbonated and chloride-contaminated concrete, the corrosion rates of steel increase significantly, especially in the range of humidity 65%–95%.[70]

For this reason, in the next subsection numerical seismic analysis of the RC piers accounting for different corrosion scenarios will be performed by incorporating mechanical characteristics and degradation phenomena identified in the experimental campaign within the proposed fiber hinge model, using the empirical relationships for uniform corrosion presented in Section 2. Although the extracted bars concerning longitudinal reinforcement (ϕ24 and ϕ20 mm diameter) did not exhibit any evident mass loss, it is reasonable to assume (postulate in the analysis) that, in addition to stirrups, also longitudinal bars may be statistically affected by corrosion-induced degradation.

5.4 | Numerical seismic analysis: Response spectrum, nonlinear static and nonlinear dynamic analysis

According to other literature studies,[74] the seismic behavior is numerically analyzed based on the "Individual pier model" allowed by §4.2.2.6 of Eurocode 8-Part 2 (EC8-2) provisions[75]: this simplified model is supported by the straight configuration in the longitudinal direction and the relatively comparative height of the piers (apart from those near the abutments). Hence, a cantilever beam model was used to describe the longitudinal and transverse behavior of the piers, with a distributed pier mass along the height and a point mass at the top representing the tributary mass resulting from the deck and the pier cap. More refined models including explicitly the superstructure and accounting for interaction between adjacent piers will be studied in future work. Slab action and localized membrane effects in the corners of cross section are also neglected by the proposed beam-bending model and could be taken into account by more refined shell formulations in follow-up studies.

The experimental findings from in-situ tests are used to calibrate the fiber-hinge model and to perform the seismic vulnerability assessment accounting for corrosion-induced degradation. The analyses are performed on one of the piers lying in the central part of the viaduct (height 40.14 m), discretized in 14 beam elements of variable length (Figure 15a). The pier is subject to an axial force at its top in the seismic design situation $N_{top} = 10.97$ MN, which corresponds to an axial force at its base (including self-weight) $N_{Ed} = 19.75$ MN. Cross-sectional characteristics are implemented through the Section Designer utility built in SAP2000[54] (Figure 15b), by adopting the corrosion-induced degradation laws illustrated in Section 3 ($\beta_{F_y} = \beta_{F_u} = 0.014$ in Equation (6) and $\widehat{\beta}_{\varepsilon_{su}} = 0.0277$ in the second of Equation (7)). Although different confinement portions of the section are explicitly considered in the model (different colors of concrete areas in Figure 15b, which corresponds to different confinement factors in the Mander et al. model[56] depending on the amount and distance of angular bars, brackets and stirrups), the differences between unconfined and confined concrete are almost negligible (Figure 15c) due to the large distance of brackets and the large spacing of transverse reinforcement (average value identified from pachometer tests 27 cm).

Considering the variability of the corrosion degradation observed in the experimental campaign among the different piers, three scenarios are comparatively investigated:

- uncorroded RC pier (reference case), by adopting mean material strength parameters for concrete and steel bars (for both ϕ24 mm diameter longitudinal bars and ϕ12 mm stirrups);
- corrosion scenario (1) characterized by corroded stirrups with properties obtained by the mean values of the four ϕ12* mm bars in Table 4, corroded longitudinal bars with a uniform mass loss $\Delta m = 20\%$ for all the 124 longitudinal bars along the cortical part of the section (outer perimeter) and corresponding corrosion-induced degradation of compressive strength in concrete cover, whereas the remaining 148 longitudinal bars in the internal side of the section are assumed with the uncorroded mechanical properties (mean values from the ϕ24 mm bars in Table 4);
- corrosion scenario (2), identical to the previous corrosion scenario (1) but with $\Delta m = 30\%$ in place of $\Delta m = 20\%$.

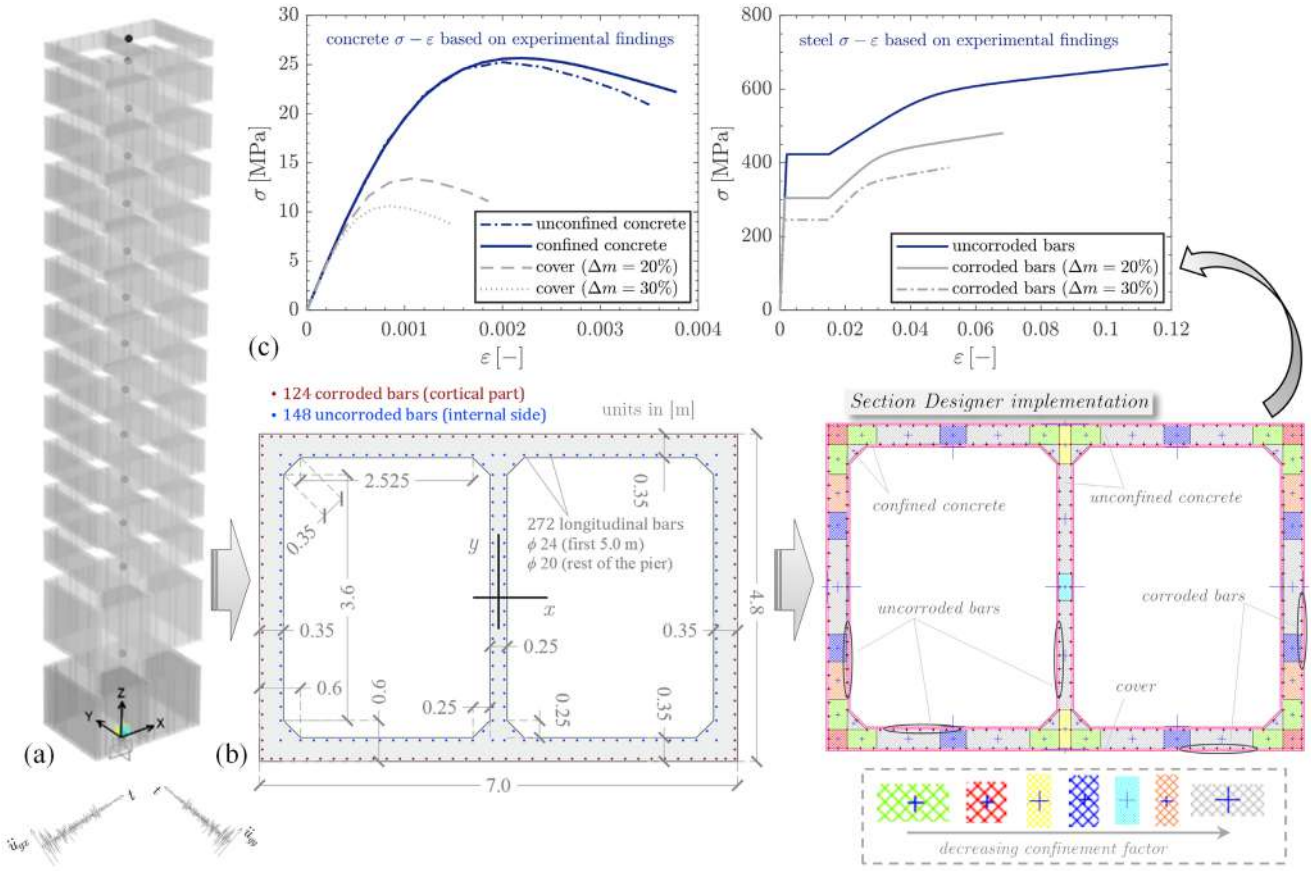

FIGURE 15 Finite element model of the reinforced concrete pier with modeling assumptions for corroded bars and concrete

Relevant stress–strain relationships for the materials in the three scenarios are depicted in Figure 15c.

First, response spectrum (linear dynamic) analysis is carried out (behavior factor $q = 1.5$, as per §4.1.6 EC8-2[75]) The site elastic response spectrum (latitude 38.1095°, longitude 14.7222°, ground type B, importance factor $\gamma_I = 2.0$) along with 14 (7 pairs) natural spectrum-compatible records selected through the software REXEL v. 3.5[76] (used afterwards for nonlinear dynamic analyses) are shown in Figure 16. Elastic flexural and shear stiffness properties of cracked concrete are assumed one-half of the corresponding stiffness terms of the uncracked elements (§4.3.1 EC8-1[61]). The resulting pier fundamental periods in the y and x direction, corresponding to the longitudinal and transverse direction of the bridge (Figure 17), are $T_1 = 1.544s$ and $T_2 = 1.186s$, respectively. Second-order effects are considered by assuming an increase of bending moment ΔM in the plastic hinge region as per §5.4 EC8-2.[75] Results from linear dynamic analyses are used to perform strength verifications in terms of $M_x - M_y - N$ interaction diagrams, thus verifying the safety inequality $E_d \leq R_d$ for all analysis and directional combinations ($E_x + 0.3E_y$ and $E_y + 0.3E_x$). In Figure 17a so-called "bending exploitation ratio" ψ can be computed as the ratio between the segment $\overline{OA}$ (representing the design value of bending demand) and the segment $\overline{OB}$ (representing the corresponding bending capacity, with B denoting the point lying on the interaction diagram along the direction defined by the segment $\overline{OA}$). Based on the ratios ψ obtained in the uncorroded scenario ($\psi = 0.476$ and $\psi = 0.704$), a relatively acceptable safety margin (around 50% and 30% in the two directions, respectively) is found; incorporating the corrosion-induced degradation leads to an obvious increase of ψ, up to around 12%–15% in the corrosion scenario (1) ($\Delta m = 20\%$) and up to 20%–24% in the corrosion scenario (2) ($\Delta m = 30\%$).

Since the participating mass ratios in the two directions is around 80% for y and x directions (first and second mode, respectively), the response of the pier to horizontal seismic action is reasonably approximated by a single-degree-of-freedom (SDoF) system. Consequently, a nonlinear static analysis is performed under the first mode load distribution. Second order effects are accounted for explicitly in the analysis. The plastic hinge length is set equal to $L_p = 5.2$ m, in accordance with NTC2018.[64] The pier capacity curves under bidirectional pushover analyses[77] for the different corrosion scenarios are shown in Figure 18. The lateral capacity of the

corroded pier (maximum base shear) decreases of 12%–14% for corrosion scenario (1) and of 16%–18% for corrosion scenario (2). As expected, the displacement ductility of the pier is higher along the *y* (weak) direction than along the *x* (rigid) direction. All the load drops in the pushover curve, in both directional combinations, correspond to the attainment of ultimate concrete strain in progressive portions of the cross section, starting from the extreme compressed fiber (section edge) inwards, whereas the tensile strain in the fibers corresponding to

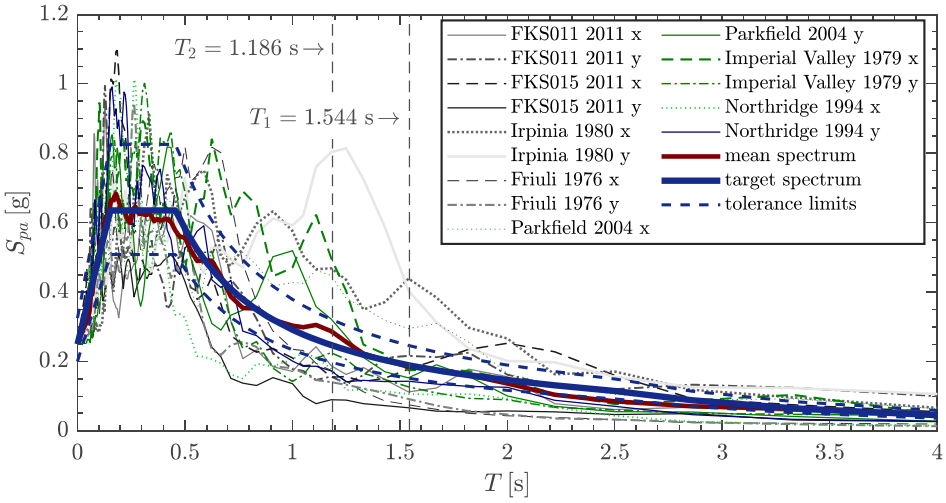

FIGURE 16 Elastic response spectrum of the site and spectrum matching criterion for 14 natural records

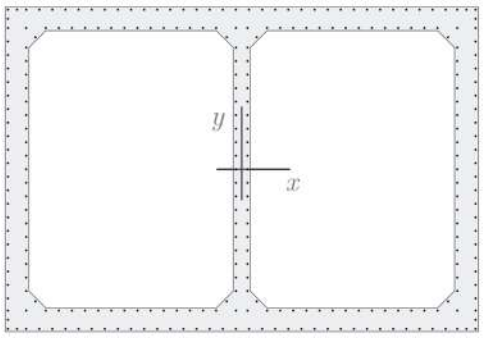

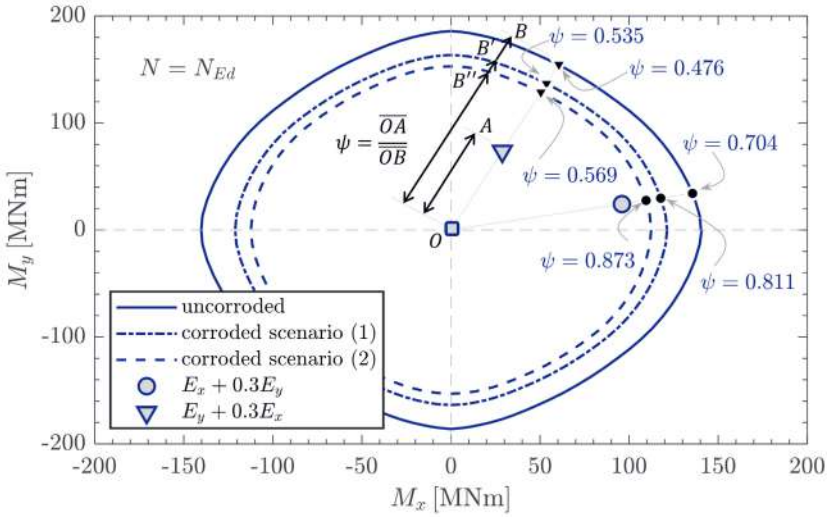

FIGURE 17 Strength verifications for base section of RC pier in terms of interaction domains for response spectrum method (linear dynamic analysis) under different corrosion scenarios

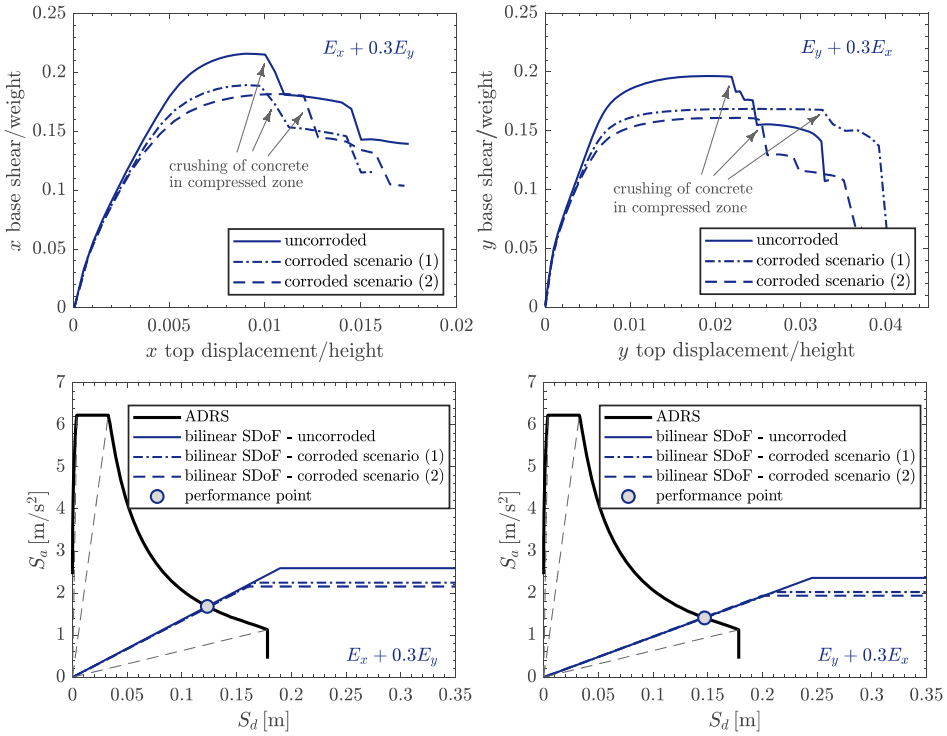

FIGURE 18 Capacity curves of RC pier for the two directional combinations under different corrosion scenarios (top) and identification of performance point in the ADRS graph (bottom)

steel reinforcement is well below the ultimate strain ε_{su}, even accounting for reduction factors $\widehat{\beta}_{\varepsilon_{su}}$ in the corroded bars. Since the dominant failure mode is ascribed to concrete crushing in the compressed zone, the degradation of mechanical properties and the reduction of resisting area of corroded steel reinforcement has led to an increase of the pier's deformation capacity, that is, a larger displacement at peak load (see pushover curves of uncorroded and corroded piers in Figure 18), even though the corroded reinforcement has approximately 50% less ductility (cf. again Figure 15c). This result can be interpreted by performing a sectional analysis in the two principal axes of the cross sections x and y, that is, strong and weak axis, respectively. In Figure 19, it can be observed that, for both axes, the peak bending moment is reached when ultimate concrete strain is reached. Looking at the strain profile at peak moment for uncorroded and corroded piers comparatively, we note that, for both axes, the neutral axis depth decreases (the compressed zone is reduced) passing from the uncorroded to the corroded case, and the steel strain in the tensile zone must increase accordingly to satisfy the equilibrium with the external actions. This, in turn, implies that a larger portion of the plastic branch of the steel constitutive relationship is exploited in the corroded scenarios. Even in the most stressed condition corresponding to weak (y) axis and corrosion scenario (2), the longitudinal tensile strain at peak moment (around 40‰) remains below the ultimate (reduced) strain of steel (higher than 50‰, cf. again Figure 15c). The displacement of the performance point evaluated according to Annex B EC8-1[61] for the uncorroded pier is $d_{target,x} = 13.55$cm and $d_{target,y} = 16.18$cm for the two directional combinations, respectively. Displacement demand of the corroded piers is comparable to that of the uncorroded case, as the intersection point in the ADRS spectrum lies along the elastic branch of the idealized pushover curve of the equivalent idealized SDoF (period $T^* = 1.7$ s and 2.03 s in the dominant x and y directions, respectively), cf. Figure 18. This displacement demand is, however, much lower than the displacement capacity of the pier even in the worst corrosion scenario (2).

Finally, nonlinear dynamic analysis is performed under the seven pairs of spectrum-compatible natural records previously shown in Figure 16. Rayleigh damping is implemented such that a damping ratio 0.05 is associated with $T = 0.2$s and 2.0s. The obtained maximum bending moments at the base of the pier are illustrated in Figure 20 and critically interpreted in relationship to the interaction diagrams.

The ratio ψ is computed for the design value of the action effects (average of the individual responses as per §4.2.4.3 EC8-2[75]) for each directional combination and corrosion scenario. Although the incorporation of corrosion-induced degradation of material properties leads to slight lengthening the effective period, thus bringing the structure to a region of reasonably lower spectral accelerations, such reduction of seismic demand

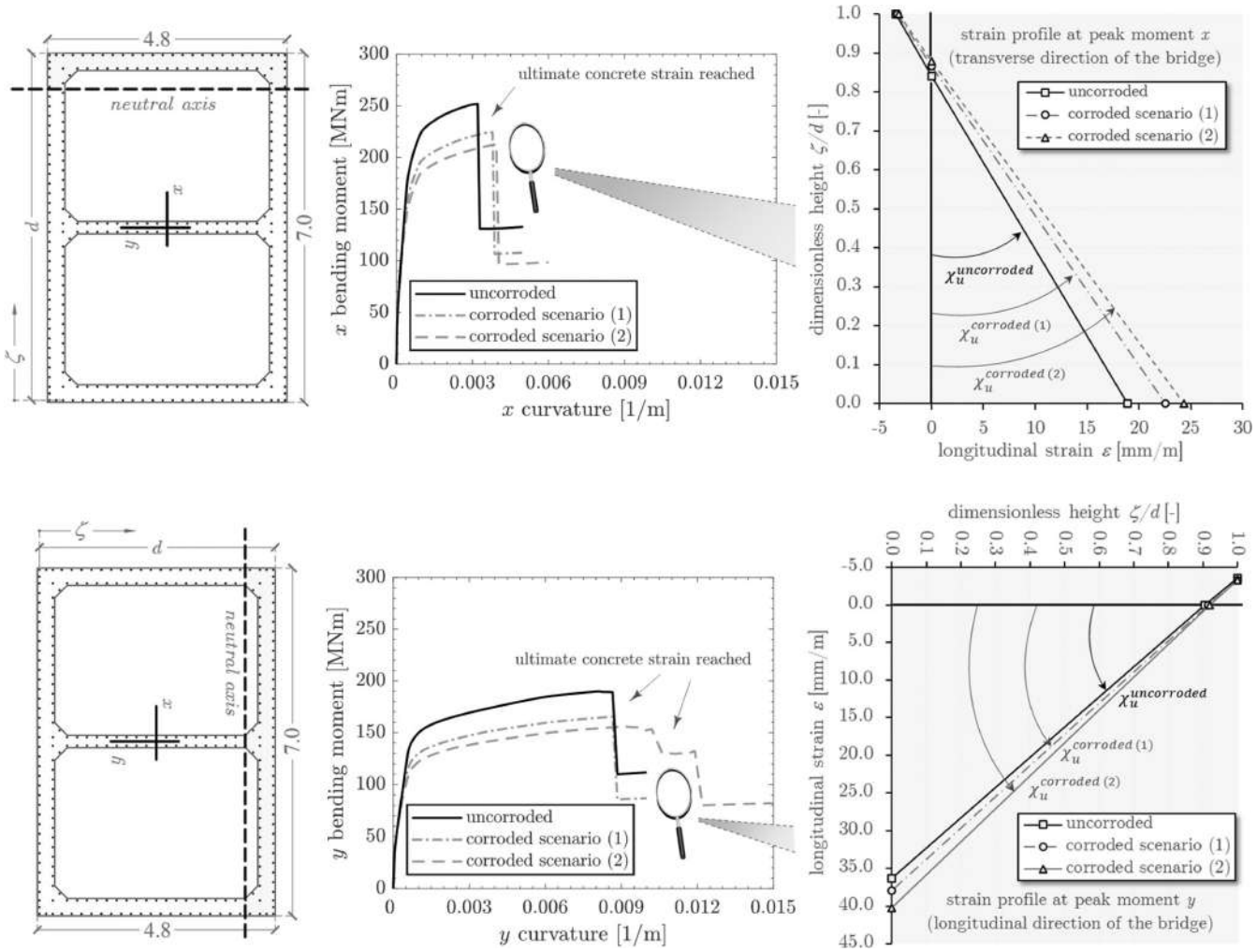

FIGURE 19 Moment-curvature relationships for base section of RC piers along the two principal axes and corresponding strain profile at peak moment in uncorroded and corroded scenarios

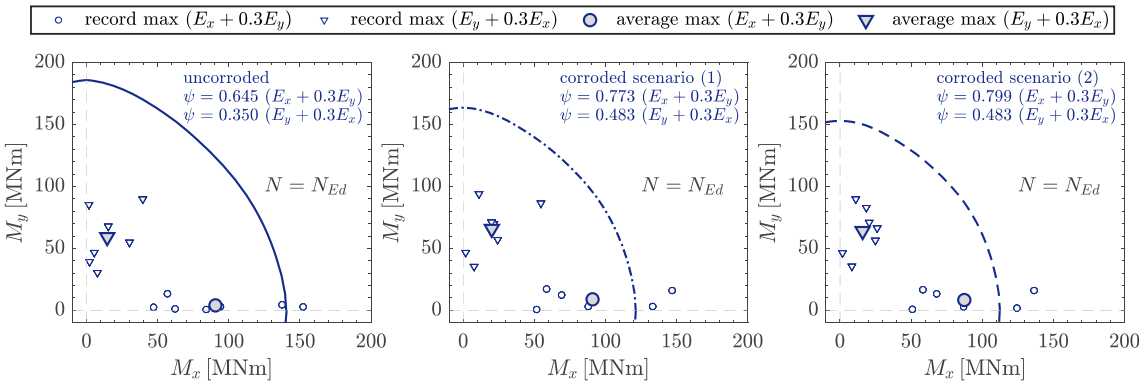

FIGURE 20 Strength verifications for base section of RC pier based on interaction domains for nonlinear dynamic analysis under different corrosion scenarios

is generally outweighed by the narrowing of the strength interaction domain. Consequently, the ratios ψ increase from the uncorroded to the corroded case, with increase percentages of around 20% and 38% for corrosion scenario (1) and of around 24% and 38% for corrosion scenario (2) in the two directional combinations, respectively. The bending exploitation ratios obtained for nonlinear dynamic analysis are, in general, 10%–20% lower than

those identified by the simplified linear dynamic analysis, which is symptomatic of the fact that, as well known, the response spectrum method is a conservative analysis approach.

6 | CONCLUSIONS AND FUTURE DEVELOPMENTS

A simple yet efficient phenomenological approach for the seismic vulnerability assessment of RC bridge piers with corroded bars has been developed. The proposed approach is based on a fiber hinge formulation, in which corrosion-induced mechanical degradation of concrete and steel reinforcing bars is implemented at the fiber level through appropriate empirical relationships from the literature. This approach has been validated against experimental cyclic tests on RC columns (uncorroded and with corroded longitudinal bars having a known, experimentally identified corrosion degree) in terms of overall hysteretic behavior, namely backbone, maximum force, strength degradation during repeated cycles and energy dissipation. It has been found that the fiber hinge model provides results that are consistent with experimental findings, and a good agreement has been observed in terms of hysteretic behavior.

Hence, the model has been applied to the Zappulla multi-span viaduct (southern Italy), whose RC piers, with box-shaped, two-cell hollow rectangular cross section, are experiencing evident corrosion-induced degradation. For this case study, a comprehensive experimental campaign has been designed and executed. Experimental results from various sources (carbonation tests, corrosion potential mapping and extraction of steel bars for tensile tests) are interpreted critically, in an interconnected manner, to identify the level of corrosion of the various piers. Average mass loss of stirrups ranging from 12% to 42% has been found from the extracted bars. Test results from the experimental campaign are used to calibrate the constitutive laws of the fiber-hinge model. Numerical seismic analysis of the piers is performed considering two corrosion scenarios to quantify the impact of corrosion on the bridge safety conditions under seismic loading. It has been found that an adequate safety margin exists in the uncorroded scenario (around 35% and 65% for the dominant seismic action along the transverse and longitudinal direction of the bridge, respectively). This scenario may be interpreted as the original condition of the piers prior to any degradation phenomenon. This safety margin decreases of 20%–40% when considering a corrosion state of reinforcing bars placed along the cortical part of the section with mass loss $\Delta m = 20\%–30\%$, whose value has been postulated in the analysis scenario on the basis of the aforementioned experimentally detected corrosion state of neighboring stirrups. Although the corroded reinforcement has approximately 50% less ductility, the degradation of mechanical properties and the reduction of resisting area of corroded steel reinforcement have led to an increase of the pier's deformation capacity, that is, a larger displacement at peak load, because the dominant failure mode is ascribed to concrete crushing in the compressed zone and not to rupture of steel bars.

The proposed model, characterized by low computational cost and a relatively feasible number of material parameters to be calibrated, lends itself to large-scale seismic vulnerability assessment of other existing RC bridges placed in corrosive environment. As demonstrated in this paper, the model can provide a first estimate of the impact of corrosion on the resulting seismic vulnerability conditions of bridge piers with corroded bars.

Some corrosion-induced phenomena could be included in future extensions of this model, such as the bond strength deterioration, buckling of compressed corroded bars and flexure-shear interaction. It would be, in principle, possible to include buckling behavior in tailored (asymmetric in tension and compression) stress–strain laws for longitudinal bars. Considering that the shear reinforcement is usually located in the outermost part of the section of RC elements (piers), the mass loss of stirrups is generally higher than that of longitudinal bars and the corresponding corrosion-induced mechanical degradation is more marked, as also confirmed by test results discussed in this experimental campaign. From this perspective, originally ductile-designed elements, like the RC piers considered in this work, could shift to a hybrid flexure-shear failure. This potential risk is further amplified by the fact that stirrups spacing originally reported in design drawings is not always put into practice in real structures. As an example, pachometer tests performed in this experimental campaign revealed that stirrups spacings of 20 cm reported in design drawings are largely underestimated by actual values detected in situ, ranging from 19 to 38 cm with a mean value of 27 cm (CoV 16.6%). In this regard, empirically calibrated shear nonlinear springs[78] can be considered in future refinements of the proposed fiber hinge model to account for coupled shear-flexure interaction behavior of corroded bridge piers.

ACKNOWLEDGMENTS

The support from the Italian High Council of Public Works (CC.SS.LL.PP.) and the Network of University Laboratories of Seismic Engineering (RELUIS) is gratefully acknowledged. The results of this study are part of the national agreement for implementing the agreement pursuant to art. 15 law 7 August 1990, No. 241 between the CC.SS.LL.PP. and RELUIS. Open Access Funding

provided by Universita degli Studi di Messina within the CRUI-CARE Agreement.

DATA AVAILABILITY STATEMENT

The data that support the findings of this study are available from the corresponding author upon reasonable request.

ORCID

Dario De Domenico https://orcid.org/0000-0003-1279-9529
Davide Messina https://orcid.org/0000-0003-2502-8520

REFERENCES

1. Lee HS, Kage T, Noguchi T, Tomosawa F. An experimental study on the retrofitting effects of reinforced concrete columns damaged by rebar corrosion strengthened with carbon fiber sheets. Cem Concr Res. 2003;33:563–70. https://doi.org/10.1016/S0008-8846(02)01004-9
2. Yang SY, Song XB, Jia HX, Chen X, La LX. Experimental research on hysteretic behaviors of corroded reinforced concrete columns with different maximum amounts of corrosion of rebar. Construct Build Mater. 2016;121:319–27. https://doi.org/10.1016/j.conbuildmat.2016.06.002
3. Guo A, Li H, Ba X, Guan X, Li H. Experimental investigation on the cyclic performance of reinforced concrete piers with chloride-induced corrosion in marine environment. Eng Struct. 2015;105:1–11. https://doi.org/10.1016/j.engstruct.2015.09.031
4. Ma Y, Che Y, Gong J. Behavior of corrosion damaged circular reinforced concrete columns under cyclic loading. Construct Build Mater. 2012;29:548–56. https://doi.org/10.1016/j.conbuildmat.2011.11.002
5. Meda A, Mostosi S, Rinaldi Z, Riva P. Experimental evaluation of the corrosion influence on the cyclic behaviour of RC columns. Eng Struct. 2014;76:112–23. https://doi.org/10.1016/j.engstruct.2014.06.043
6. Rajput AS, Sharma UK. Corroded reinforced concrete columns under simulated seismic loading. Eng Struct. 2018;171:453–63. https://doi.org/10.1016/j.engstruct.2018.05.097
7. Di Sarno L, Pugliese F. Numerical evaluation of the seismic performance of existing reinforced concrete buildings with corroded smooth rebars. Bull Earthq Eng. 2020;18:4227–73. https://doi.org/10.1007/s10518-020-00854-8
8. Zhang M, Liu R, Li Y, Zhao G. Seismic performance of a corroded reinforce concrete frame structure using pushover method. Adv Civ Eng. 2018;2018:1–12. https://doi.org/10.1155/2018/7208031
9. Li H, Li L, Zhou G, Xu L. Time-dependent seismic fragility assessment for aging highway bridges subject to non-uniform chloride-induced corrosion. J Earthq Eng. 2020;26:3523–53. https://doi.org/10.1080/13632469.2020.1809561
10. Xu JG, Wu G, Feng DC, Cotsovos DM, Lu Y. Seismic fragility analysis of shear-critical concrete columns considering corrosion induced deterioration effects. Soil Dyn Earthq Eng. 2020;134:106165. https://doi.org/10.1016/j.soildyn.2020.106165
11. Domaneschi M, De Gaetano A, Casas JR, Cimellaro GP. Deteriorated seismic capacity assessment of reinforced concrete bridge piers in corrosive environment. Struct Concr. 2020;21:1823–38. https://doi.org/10.1002/suco.202000106
12. Cui F, Zhang H, Ghosn M, Xu Y. Seismic fragility analysis of deteriorating RC bridge substructures subject to marine chloride-induced corrosion. Eng Struct. 2018;155:61–72. https://doi.org/10.1016/j.engstruct.2017.10.067
13. Tuutti K. Corrosion of steel in concrete. Swedish: Cem Betonginst; 1982.
14. Pelle A, Briseghella B, Bergami AV, Fiorentino G, Giaccu GF, Lavorato D, et al. Time-dependent cyclic behavior of reinforced concrete bridge columns under chlorides-induced corrosion and rebars buckling. Struct Concr. 2021;23:81–103. https://doi.org/10.1002/suco.202100257
15. Allam IM, Maslehuddin M, Saricimen H, Al-Mana AI. Influence of atmospheric corrosion on the mechanical properties of reinforcing steel. Construct Build Mater. 1994;8:35–41. https://doi.org/10.1016/0950-0618(94)90006-X
16. Cairns J, Plizzari GA, Du Y, Law DW, Franzoni C. Mechanical properties of corrosion-damaged reinforcement. ACI Mater J. 2005;102:256–64. https://doi.org/10.14359/14619
17. Palsson R, Mirza MS. Mechanical response of corroded steel reinforcement of abandoned concrete bridge. ACI Struct J. 2002;99:157–62. https://doi.org/10.14359/11538
18. Maslehuddin M, Allam IM, Al-Sulaimani GJ, Al-Mana A, Abduljauwad SN. Effect of rusting of reinforcing steel on its mechanical properties and bond with concrete. ACI Mater J. 1990;87:496–502. https://doi.org/10.14359/1902
19. Zhang W, Song X, Gu X, Li S. Tensile and fatigue behavior of corroded rebars. Construct Build Mater. 2012;34:409–17. https://doi.org/10.1016/j.conbuildmat.2012.02.071
20. Lee HS, Tomosawa F, Noguchi T. Effect of rebar corrosion on the structural performance of singly reinforced beams. In: Spon E, Sjöström C, editors. Durab. Build. Mater. Volume 7. Sweden, London, U.K: components, Stock; 1996. p. 571–80.
21. Apostolopoulos CA, Papadopoulos MP, Pantelakis SG. Tensile behavior of corroded reinforcing steel bars BSt 500 s. Construct Build Mater. 2006;20:782–9. https://doi.org/10.1016/j.conbuildmat.2005.01.065
22. Apostolopoulos CA. Mechanical behavior of corroded reinforcing steel bars S500s tempcore under low cycle fatigue. Construct Build Mater. 2007;21:1447–56. https://doi.org/10.1016/j.conbuildmat.2006.07.008
23. Andisheh K, Scott A, Palermo A. Modeling the influence of pitting corrosion on the mechanical properties of steel reinforcement. Mater Corros. 2016;67:1220–34. https://doi.org/10.1002/maco.201508795
24. Finozzi I, Saetta A, Budelmann H. Structural response of reinforcing bars affected by pitting corrosion: experimental evaluation. Construct Build Mater. 2018;192:478–88. https://doi.org/10.1016/j.conbuildmat.2018.10.088
25. Fernandez I, Bairán JM, Marí AR. Corrosion effects on the mechanical properties of reinforcing steel bars. Fatigue and σ-ε behavior. Construct Build Mater. 2015;101:772–83. https://doi.org/10.1016/j.conbuildmat.2015.10.139
26. Oyado M, Kanakubo T, Sato T, Yamamoto Y. Bending performance of reinforced concrete member deteriorated by

corrosion. Struct Infrastruct Eng. 2011;7:121–30. https://doi.org/10.1080/15732471003588510
27. Castel A, François R, Arliguie G. Mechanical behaviour of corroded reinforced concrete beams—part 1: experimental study of corroded beams. Mater Struct Constr. 2000;33:539–44. https://doi.org/10.1007/bf02480533
28. Morinaga S. Remaining service life of reinforced concrete structure after corrosion cracking. In: Spon FN, Sjöström C, editors. Durab. Build. Mater. Volume 1. Sweden, London, U.K: components, Stock; 1996. p. 127–37.
29. Du YG, Clark LA, Chan AHC. Residual capacity of corroded reinforcing bars. Mag Concr Res. 2005;57:135–47. https://doi.org/10.1680/macr.2005.57.3.135
30. Zhu W, François R, Poon CS, Dai JG. Influences of corrosion degree and corrosion morphology on the ductility of steel reinforcement. Construct Build Mater. 2017;148:297–306. https://doi.org/10.1016/j.conbuildmat.2017.05.079
31. Chen E, Berrocal CG, Fernandez I, Löfgren I, Lundgren K. Assessment of the mechanical behaviour of reinforcement bars with localised pitting corrosion by digital image correlation. Eng Struct. 2020;219:110936. https://doi.org/10.1016/j.engstruct.2020.110936
32. Du YG, Clarkt LA, Chan AHC. Effect of corrosion on ductility of reinforcing bars. Mag Concr Res. 2005;57:407–19. https://doi.org/10.1680/macr.2005.57.7.407
33. Kashani MM, Crewe AJ, Alexander NA. Nonlinear stress-strain behaviour of corrosion-damaged reinforcing bars including inelastic buckling. Eng Struct. 2013;48:417–29. https://doi.org/10.1016/j.engstruct.2012.09.034
34. Lavorato D, Fiorentino G, Pelle A, Rasulo A, Bergami AV, Briseghella B, et al. A corrosion model for the interpretation of cyclic behavior of reinforced concrete sections. Struct Concr. 2020;21:1732–46. https://doi.org/10.1002/suco.201900232
35. Coronelli D, Gambarova P. Structural assessment of corroded reinforced concrete beams: modeling guidelines. J Struct Eng. 2004;130:1214–24. https://doi.org/10.1061/(asce)0733-9445(2004)130:8(1214)
36. Vidal T, Castel A, François R. Analyzing crack width to predict corrosion in reinforced concrete. Cem Concr Res. 2004;34:165–74. https://doi.org/10.1016/S0008-8846(03)00246-1
37. Andrade C, Cesetti A, Mancini G, Tondolo F. Estimating corrosion attack in reinforced concrete by means of crack opening. Struct Concr. 2016;17:533–40. https://doi.org/10.1002/suco.201500114
38. Torres-Acosta AA, Martínez-Madrid M. Residual life of corroding reinforced concrete structures in marine environment. J Mater Civ Eng. 2003;15:344–53. https://doi.org/10.1061/(asce)0899-1561(2003)15:4(344)
39. Molina FJ, Alonso C, Andrade C. Cover cracking as a function of rebar corrosion: part 2-numerical model. Mater Struct. 1993;26:532–48. https://doi.org/10.1007/BF02472864
40. Coccia S, Imperatore S, Rinaldi Z. Influence of corrosion on the bond strength of steel rebars in concrete. Mater Struct Constr. 2016;49:537–51. https://doi.org/10.1617/s11527-014-0518-x
41. Mancini G, Tondolo F. Effect of bond degradation due to corrosion—a literature survey. Struct Concr. 2014;15:408–18. https://doi.org/10.1002/suco.201300009
42. ASTM Standard G1-90. Standard Practice for Preparing, Cleaning, and Evaluating Corrosion Test Specimens. 1999.
43. Val DV, Melchers RE. Reliability of deteriorating RC slab bridges. J Struct Eng. 1997;123:1638–44. https://doi.org/10.1061/(asce)0733-9445(1997)123:12(1638)
44. González JA, Andrade C, Alonso C, Feliu S. Comparison of rates of general corrosion and maximum pitting penetration on concrete embedded steel reinforcement. Cem Concr Res. 1995;25:257–64. https://doi.org/10.1016/0008-8846(95)00006-2
45. Kagermanov A, Markovic I. An overview on finite element-modelling techniques for structural capacity assessment of corroded reinforced concrete structures. Struct Infrastruct Eng. 2022;1–15. https://doi.org/10.1080/15732479.2022.2045612
46. Zeng C, Zhu JH, Xiong C, Li Y, Li D, Walraven J. Analytical model for the prediction of the tensile behaviour of corroded steel bars. Construct Build Mater. 2020;258:120290. https://doi.org/10.1016/j.conbuildmat.2020.120290
47. Imperatore S, Rinaldi Z, Drago C. Degradation relationships for the mechanical properties of corroded steel rebars. Construct Build Mater. 2017;148:219–30. https://doi.org/10.1016/j.conbuildmat.2017.04.209
48. Kashani MM, Crewe AJ, Alexander NA. Use of a 3D optical measurement technique for stochastic corrosion pattern analysis of reinforcing bars subjected to accelerated corrosion. Corros Sci. 2013;73:208–21. https://doi.org/10.1016/j.corsci.2013.03.037
49. Li D, Wei R, Li L, Guan X, Mi X. Pitting corrosion of reinforcing steel bars in chloride contaminated concrete. Construct Build Mater. 2019;199:359–68. https://doi.org/10.1016/j.conbuildmat.2018.12.003
50. Imperatore S. Mechanical properties decay of corroded reinforcement in concrete—an overview. Corros Mater Degrad. 2022;3:210–20. https://doi.org/10.3390/cmd3020012
51. Lee HS, Cho YS. Evaluation of the mechanical properties of steel reinforcement embedded in concrete specimen as a function of the degree of reinforcement corrosion. Int J Fract. 2009;157:81–8. https://doi.org/10.1007/s10704-009-9334-7
52. Vecchio FJ, Collins MP. The modified compression field theory for RC elements subjected to shear. J Am Concr Inst. 1986;83:219–31. https://doi.org/10.14359/10416
53. ACI Committee 374.1. Acceptance Criteria for Moment Frames Based on Structural Testing and Commentary: An ACI Standard. 2005.
54. Computers and Structures Inc. CSi analysis reference manual for SAP2000®. Berkeley: CA, USA; 2016.
55. Park R, Paulay T. Reinforced concrete structures. Ltd: John Wiley & Sons; 1975.
56. Mander JB, Priestley MJN, Park R. Theoretical stress-strain model for confined concrete. J Struct Eng. 1988;114:1804–26. https://doi.org/10.1061/(asce)0733-9445(1988)114:8(1804)
57. Haefliger S, Kaufmann W. Influence of cross section loss on the stress-strain characteristics of corroded quenched and self-tempered reinforcing bars. Construct Build Mater. 2021;282:122598. https://doi.org/10.1016/j.conbuildmat.2021.122598
58. Fernandez I, Bairán JM, Marí AR. Mechanical model to evaluate steel reinforcement corrosion effects on σ-ε and fatigue curves experimental calibration and validation. Eng Struct. 2016;118:320–33. https://doi.org/10.1016/j.engstruct.2016.03.055
59. Boeraeve P, Lognard B, Janss J, Gérardy JC, Schleich JB. Elasto-plastic behaviour of steel frame works. J Constr Steel Res. 1993;27:3–21. https://doi.org/10.1016/0143-974X(93)90003-B
60. Cosenza E, Manfredi G, Verderame GM, Ricci P, De Carlo G, Masi A. Capacity models of RC members with emphasis on sub-standard columns with plain bars. Eurocode 8 Perspect. From Ital. Standpoint work. Doppiavoce, Napoli, Italy; 2009. p. 129–44.

61. European Committee for Standardization. Eurocode 8: design of structures for earthquake resistance—part 1: general rules, seismic actions and rules for buildings. EN 1998-1:2004+A1: 2013. Brussels, Belgium; 2004.
62. De Domenico D, Messina D, Recupero A. Quality control and safety assessment of prestressed concrete bridge decks through combined field tests and numerical simulation. Structure. 2022; 39:1135–57. https://doi.org/10.1016/j.istruc.2022.03.086
63. Verderame GM, Ricci P, Esposito M, Sansiviero F. Le caratteristiche meccaniche degli acciai impiegati nelle strutture in ca realizzate dal 1950 al 1980. XXVI Convegno Naz AICAP. 2011;2011: 1–8.
64. Italian Ministry of Infrastructures and Transportations. NTC2018. Aggiornamento delle «Norme tecniche per le costruzioni» Decreto 17 Gennaio 2018, Supplemento ordinario alla Gazzetta ufficiale n. 42, 20 February 2018 (In Italian). 2018.
65. Dewar J, Collis L, Llewellin J, Murphy W, Plowman JM, Warren PA, et al. Concrete core testing for strength. Technical report n.11 of a concrete society working party. London, U.K: Concrete Society; 1987.
66. International Atomic Energy Agency (IAEA). Guidebook on non-destructive testing of concrete structures. Vol 17. Vienna, Austria: Training Course Series; 2002.
67. Cristofaro MT, Viti S, Tanganelli M. New predictive models to evaluate concrete compressive strength using the SonReb method. J Build Eng. 2020;27:100962. https://doi.org/10.1016/J.JOBE.2019.100962
68. fib Commission 3 Existing concrete structures. CEB-fib Bulletin 80, Partial factor methods for existing concrete structures. Recommendation Task Group 3.1. Germany: 2016.
69. Yun X, Gardner L. Stress-strain curves for hot-rolled steels. J Constr Steel Res. 2017;133:36–46. https://doi.org/10.1016/j.jcsr.2017.01.024
70. Bertolini L, Elsener B, Pedeferri P, Polder R. Corrosion of steel in concrete: prevention, diagnosis, repair. Weinheim, Germany: WILEY-VCH Verlag GmbH & Co. KGaA; 2005. https://doi.org/10.1002/3527603379
71. Gulikers J, Elsener B. Development of a calculation procedure for the statistical interpretation of the results of potential mapping performed on reinforced concrete structures. Mater Corros. 2009;60:87–92. https://doi.org/10.1002/maco.200805089
72. American Society for Testing and Materials. ASTM C 876/91—standard test method for half-cell potentials of uncoated reinforcing steel in concrete. West Conshohocken, PA: ASTM; 1991.
73. Pedeferri P, Bertolini L. La corrosione nel calcestruzzo e negli ambienti naturali. 1st ed. Milan, Italy: McGraw-Hill Italia; 1996.
74. Tubaldi E, Scozzese F, De Domenico D, Dall'Asta A. Effects of axial loads and higher order modes on the seismic response of tall bridge piers. Eng Struct. 2021;247:113134. https://doi.org/10.1016/j.engstruct.2021.113134
75. European Committee for Standardization. Eurocode 8—design of structures for earthquake resistance—part 2: bridges. EN 1998-2:2005+A2:2011. Brussels, Belgium; 2005.
76. Iervolino I, Galasso C, Cosenza E. REXEL: computer aided record selection for code-based seismic structural analysis. Bull Earthq Eng. 2010;8:339–62. https://doi.org/10.1007/s10518-009-9146-1
77. Cimellaro GP, Giovine T, Lopez-Garcia D. Bidirectional push-over analysis of irregular structures. J Struct Eng. 2014;104: 04014059. https://doi.org/10.1061/(asce)st.1943-541x.0001032
78. Xu JG, Feng DC, Wu G, Cotsovos DM, Lu Y. Analytical modeling of corroded RC columns considering flexure-shear interaction for seismic performance assessment. Bull Earthq Eng. 2020;18: 2165–90. https://doi.org/10.1007/s10518-019-00770-6
79. RILEM NDT 4. Recommendation for in situ concrete strength determination by methods, combined non-destructive, compendium of RILEM technical recommendations. London, U.K: E & FN SPON; 1993.
80. Gašparik J. Prove non distruttive nell'edilizia (in Italian). Quaderno Didattico Associazione Italiana Prove Non Distruttive (AIPnD): Brescia; 1992.
81. Di Leo A, Pascale G. Prove non distruttive sulle costruzioni in cemento armato Il Giornale Delle Prove Non Distruttive Monitoraggio Diagnostica 1994;4.

AUTHOR BIOGRAPHIES

Dario De Domenico, Assistant Professor, Department of Engineering, University of Messina, Messina, Italy.
dario.dedomenico@unime.it.

Davide Messina, PhD Student, Department of Engineering, University of Messina, Messina, Italy.
davide.messina@unime.it.

Antonino Recupero, Full Professor, Department of Engineering, University of Messina, Messina, Italy.
antonino.recupero@unime.it.

How to cite this article: De Domenico D, Messina D, Recupero A. Seismic vulnerability assessment of reinforced concrete bridge piers with corroded bars. Structural Concrete. 2023;24(1): 56–83. https://doi.org/10.1002/suco.202200378